



HAL
open science

Constraining lowermost mantle anisotropy with body waves: a synthetic modelling study

Neala Creasy, Angelo Pisconti, Maureen D Long, Christine Thomas, James Wookey

► To cite this version:

Neala Creasy, Angelo Pisconti, Maureen D Long, Christine Thomas, James Wookey. Constraining lowermost mantle anisotropy with body waves: a synthetic modelling study. *Geophysical Journal International*, 2019, 217 (2), pp.766-783. 10.1093/gji/ggz049 . hal-02162789

HAL Id: hal-02162789

<https://hal.science/hal-02162789>

Submitted on 22 Jun 2019

HAL is a multi-disciplinary open access archive for the deposit and dissemination of scientific research documents, whether they are published or not. The documents may come from teaching and research institutions in France or abroad, or from public or private research centers.

L'archive ouverte pluridisciplinaire **HAL**, est destinée au dépôt et à la diffusion de documents scientifiques de niveau recherche, publiés ou non, émanant des établissements d'enseignement et de recherche français ou étrangers, des laboratoires publics ou privés.

1
2
3 **Constraining lowermost mantle anisotropy with body waves: A synthetic modeling**
4 **study**

5
6 Neala Creasy^{1*}, Angelo Pisconti², Maureen D. Long¹, Christine Thomas², and
7 James Wookey³
8

9 ¹Department of Geology and Geophysics, Yale University

10 ²Institut für Geophysik, Universität Münster

11 ³Department of Earth Sciences, University of Bristol

12 *Corresponding author. Email: neala.creasy@yale.edu
13

14 This is a pre-copyedited, author-produced PDF of an article accepted for publication in
15 *Geophysical Journal International* ©: 2019 Neala Creasy
16

17
18 Published by Oxford University Press on behalf of the Royal Astronomical Society. All
19 rights reserved. The version of record
20

21 “Neala Creasy, Angelo Pisconti, Maureen D Long, Christine Thomas, James Wookey,
22 Constraining lowermost mantle anisotropy with body waves: a synthetic modelling
23 study, *Geophysical Journal International*, Volume 217, Issue 2, May 2019, Pages 766–
24 783, <https://doi.org/10.1093/gji/ggz049>”
25

26 is available online at:

27 [https://academic.oup.com/gji/article/217/2/766/5303728?guestAccessKey=ab8c43d4-
28 40ab-4b68-8e67-3ddf14272a4f](https://academic.oup.com/gji/article/217/2/766/5303728?guestAccessKey=ab8c43d4-40ab-4b68-8e67-3ddf14272a4f)
29
30
31
32

33 Summary

34 Different mechanisms have been proposed as explanations for seismic anisotropy
35 at the base of the mantle, including crystallographic preferred orientation of various
36 minerals (bridgmanite, post-perovskite, and ferropericlase) and shape preferred orientation
37 of elastically distinct materials such as partial melt. Investigations of the mechanism for
38 D" anisotropy usually yield ambiguous results, as seismic observations rarely (if ever)
39 uniquely constrain a mechanism or orientation and usually rely on significant assumptions
40 to infer flow patterns in the deep mantle. Observations of shear wave splitting and polarities
41 of SdS and PdP reflections off the D" discontinuity are among our best tools for probing
42 D" anisotropy; however, currently available datasets cannot constrain one unique scenario
43 among those suggested by the mineral physics literature. In this work, we determine via a
44 forward modeling approach what combinations of body wave phases (e.g. SKS, SKKS,
45 and ScS) are required to uniquely constrain a mechanism for D" anisotropy. We test nine
46 models based on single-crystal and polycrystalline elastic tensors provided by mineral
47 physics studies. Our modeling predicts fast shear wave splitting directions for SKS, SKKS,
48 and ScS phases, as well as polarities of P and S wave reflections off the D" interface, for a
49 range of propagation directions, via solution of the Christoffel equation. We run tests using
50 randomly selected synthetic datasets based on a given starting model, controlling the total
51 number of measurements, the azimuthal distribution, and the type of seismic phases. For
52 each synthetic dataset, we search over all possible elastic tensors and orientations to
53 determine which are consistent with the synthetic data. Overall, we find it difficult to
54 uniquely constrain the mechanism for anisotropy with a typical number of seismic
55 anisotropy measurements (based on currently available studies) with only one

56 measurement technique (SKS, SKKS, ScS, or reflection polarities). However, datasets that
57 include SKS, SKKS, and ScS measurements or a combination of shear wave splitting and
58 reflection polarity measurements increase the probability of uniquely constraining the
59 starting model and its orientation. Based on these findings, we identify specific regions
60 (i.e., North America, northwestern Pacific, and Australia) of the lowermost mantle with
61 sufficient raypath coverage for a combination of measurement techniques.

62 Abbreviated Title: Constraining lowermost mantle anisotropy

63

64 Keywords (up to 6):

- 65 • Seismic anisotropy
- 66 • Composition and structure of the mantle
- 67 • Mantle processes
- 68 • Statistical seismology

69 **1. Introduction**

70 Mantle convection finds its surface expression in plate tectonics and represents a
71 crucial dynamic process in the deep Earth. Despite its importance, the pattern of mantle
72 convection and the forces that drive mantle flow remain imperfectly understood. This is
73 particularly true for the deepest mantle: flow at the base of the mantle likely influences
74 (and/or is influenced by) structures such as large low shear velocity provinces (LLSVPs).
75 Subducting slabs likely penetrate into the lower mantle and hot mantle plumes generate
76 from or near the LLSVPs, indicating a strong connection between the surface and deep
77 mantle processes (e.g., Garnero et al., 2016).

78 Observations of seismic anisotropy have the potential to illuminate mantle flow,
79 due to the relationship between strain due to mantle convection and seismic anisotropy via
80 lattice preferred orientation (LPO) or shape preferred orientation (SPO) mechanisms. The
81 presence of anisotropy in the D" layer at the base of the mantle has been known for several
82 decades (e.g., Lay and Helmberger, 1983) from the analysis of body wave phases (as
83 summarized in Nowacki et al., 2011). At this point a relatively small fraction (Figure 1) of
84 the core mantle boundary region has been explored for D" anisotropy using body waves.
85 Figure 1 shows a map, updated from Nowacki et al. (2011) illustrating the geographical
86 coverage of previous studies (including recent work by Creasy et al., 2017, Deng et al.,
87 2017, Simmons et al., 2015, Ford et al., 2015, Long and Lynner, 2015, Lynner and Long,
88 2014, Cottaar and Romanowicz, 2013, and Thomas et al., 2011). Despite these
89 observations, however, we still do not fully understand the anisotropy in these regions.
90 Several different models for D" anisotropy have been proposed, including those that invoke
91 LPO of bridgmanite (Br), post-perovskite (Ppv), or ferropericlaase (Fp), and those that

92 invoke SPO of partial melt (see Nowacki et al., 2011 for a review). The mechanisms
93 responsible for D" anisotropy, the dominant slip systems involved, the orientation of the
94 anisotropic fabric, and the implications for mantle flow geometries thus remain poorly
95 understood.

96 A variety of body waves has been used to study anisotropy in the deepest mantle.
97 Specifically, direct S, ScS, and Sdiff have been used to observe lowermost mantle
98 anisotropy by measuring shear wave splitting (e.g., Wookey et al., 2005a, Cottaar and
99 Romanowicz, 2013, Thomas et al., 2007, Ford et al., 2006). Combinations of phases, such
100 as SKS-SKKS (e.g., Wang and Wen, 2007; Long, 2009) or S-ScS (e.g., Wookey et al.,
101 2005a; Nowacki et al., 2010), are often useful to isolate the lowermost mantle contribution
102 to splitting. Thomas et al. (2011) used an array analysis technique to observe reflected P
103 and S waves off the D" discontinuity; the azimuthal dependence of the polarity of D"
104 reflections SdS and PdP contains information about lowermost mantle anisotropy. While
105 body wave observations have been extensively used to study anisotropy at the base of the
106 mantle, such studies suffer from the fundamental limitation of small azimuthal coverage;
107 most studies are essentially restricted to a single raypath, which means that the geometry
108 of anisotropy cannot be tightly constrained.

109 Several recent studies of deep mantle anisotropy have ameliorated this limitation
110 by targeting regions of D" that are sampled by body waves over multiple azimuths (pink
111 regions in Figure 1). These include studies of the lowermost mantle beneath Siberia
112 (Wookey and Kendall, 2008; Thomas et al., 2011), North America (Nowacki et al., 2010),
113 the Afar region of Africa (Ford et al., 2015), and Australia and New Zealand (Creasy et al.,
114 2017). In some cases, one can test whether the observations could clearly distinguish

115 among different mechanisms for anisotropy. For example, Ford et al. (2015) and Creasy et
116 al. (2017) carried out forward modeling of ScS, SKS, and SKKS splitting datasets over
117 multiple azimuths to test whether a unique mechanism for anisotropy and/or a unique
118 orientation of an assumed mechanism could be identified. In each of these studies it was
119 found that LPO of Ppv matches the observations, but other mechanisms (such as LPO of
120 Br or Fp) were also consistent with the data. None of the studies summarized in Figure 1
121 has successfully identified a uniquely constrained mechanism or orientation for anisotropy.
122 Motivated by this, we attempt here to understand what observations are needed to
123 distinguish the various possible models for D'' anisotropy.

124 The goal of this study is to understand what combination of body wave datasets
125 (SKS, SKKS, ScS, and reflection polarities) are necessary to uniquely constrain the
126 mechanism and geometry of anisotropy in the lowermost mantle using observations of
127 shear wave splitting and D'' reflection polarities. Such an understanding will aid in the
128 design of future observational studies to maximize the chances of uniquely constraining a
129 mechanism. We are interested in understanding the characteristics of datasets that are best
130 suited to constrain the details of D'' anisotropy, including the number of measurements
131 needed, the optimal azimuthal coverage, and the optimal combinations of body wave
132 phases. We address two specific questions: 1) What types of datasets (potentially including
133 SKS, SKKS, and/or ScS splitting, and/or reflection polarities) are needed to uniquely
134 identify the causative mechanism for anisotropy (e.g., LPO of Ppv, Br, Fp, or SPO of partial
135 melt); and 2) if we assume that the mechanism for anisotropy is known to be LPO of Ppv,
136 what type of datasets are needed to uniquely constrain the orientation of the anisotropy?

137 We carry out forward modeling tests for a suite of synthetic body wave data. Our
138 approach to forward modeling of synthetic datasets follows our previous work on
139 observations of shear wave splitting in D'' (Ford et al., 2015; Creasy et al., 2017) and also
140 incorporates measurements of D'' polarities of P and S wave reflections (Thomas et al.,
141 2011a). Our approach is to test a variety of candidate elastic tensors that describe various
142 mechanisms for lowermost mantle anisotropy. For each model, we randomly generate more
143 than 5,000 unique synthetic datasets (for SKS, SKKS, and ScS shear wave splitting, plus
144 PdP and SdS polarities) with a certain set of characteristics (e.g., number and type of
145 measurements, as described below) and a random azimuthal distribution. For each set of
146 random raypaths, we compute a set of predicted “observations” of shear wave splitting
147 and/or reflection polarities using a ray theoretical approach. We then attempt to determine
148 what characteristics of body wave datasets are optimal for uniquely constraining anisotropy
149 in the lowermost mantle.

150

151 **2. Methods**

152 2.1 Candidate models for D'' anisotropy

153 We first consider which plausible models for D'' anisotropy should be tested. The
154 lower mantle is likely composed of pyrolite (e.g., Lee et al., 2004), a model composition
155 that consists of ~76 mol% of bridgmanite (Br: MgSiO₃), ~17 mol% of periclase (Fp:
156 (Mg,Fe)O), and ~7 mol% of calcium perovskite (Capv: CaSiO₃). In the D'' layer at the base
157 of the mantle, we expect a phase change of Br to post-perovskite (Ppv: MgSiO₃) (e.g.,
158 Murakami et al., 2004). Based on *ab initio* calculations and laboratory experiments, Br, Fp,
159 and Ppv all have strong single-crystal anisotropy, with Fp being the weakest mineral and

160 the most anisotropic (as summarized in Nowacki et al., 2011), although it is less abundant
161 than Br/Ppv. This suggests that LPO development in any of the dominant lowermost mantle
162 minerals may contribute to the observed anisotropy, as long as deformation is taking place
163 in the dislocation creep regime (e.g., McNamara et al., 2001). Another possible mechanism
164 is aligned pockets of an elastically distinct material such as partial melt in configurations
165 such as disks, tubes, or sheets, creating shape preferred orientation (SPO) (e.g., Kendall
166 and Silver, 1998) (Tables 1 and 2).

167 We test a suite of models that describe single-crystal elasticity of lowermost mantle
168 materials derived from *ab initio* calculations, following our previous modeling work (Ford
169 et al., 2015; Creasy et al., 2017). This approach assumes that an aggregate will have the
170 same anisotropic geometry (although not strength) as a single crystal. In addition to the
171 single-crystal models, we test one model (for Fp LPO) based on deformation experiments
172 (Long et al., 2006) and models that invoke the SPO (shape-preferred orientation) of partial
173 melt (Table 1), with elastic constants calculated using an implementation of effective
174 medium theory within the MSAT toolbox (Walker and Wookey, 2012).

175 Finally, our last candidate model approximates a textured Ppv aggregate and is
176 derived from a 3D, global mantle flow field calculation in combination with a visco-plastic
177 self-consistent model LPO development in Ppv (Walker et al., 2011). We determined a
178 representative elastic tensor for Ppv texture development in high-strain simple shear by
179 querying the TX2008.V1.P010 model of Walker et al. (2011), which combined a lower
180 mantle viscosity model from Mitrovica and Forte (2004) with a mantle density model from
181 Simmons et al. (2009). We only considered the case in which slip on the (010) plane
182 dominates; this is the most likely slip plane for Ppv based on experiments (Walte et al.,

183 2009; Yamazaki et al., 2006), modeling (Goryaeva et al., 2017), and observations of D"
184 anisotropy (Creasy et al., 2017; Ford et al., 2015; Thomas et al., 2011). To obtain a
185 representative average tensor for simple shear, we identified a 15° by 15° geographical
186 region of the global flow (beneath the northern Atlantic Ocean) that is dominated by strong
187 horizontal shear. We then extracted and averaged the 16 elastic tensors (the model
188 calculated tensors every 5°) from the resulting TX2008.V1.P010 elasticity predictions in
189 this region.

190

191 2.2 Computation of reflection polarities and fast splitting directions

192 Given the full suite of candidate models for elasticity in D'' to be used in our study
193 (Table 1), we implement methods for predicting various types of body wave observations
194 for these scenarios. We calculated predicted shear wave splitting fast directions for SKS,
195 SKKS, and ScS phases (Figure 2) over a range of azimuths (every 5°) and inclinations for
196 each of these models (Tables 1) by solving the Christoffel equation using the MSAT toolkit
197 of Walker and Wookey (2012). The three different phases propagate at different inclination
198 angles: ~55°, 35°, 0° from the horizontal, respectively.

199 We then calculated the reflection polarities of SdS and PdP and the corresponding
200 predicted shear wave splitting fast directions (Figure 3) over a range of azimuths (every
201 5°) and inclinations for each of these models (Tables 1 and 2). Table 2 summarizes the
202 models used to generate predictions of D'' reflection polarities (SdS and PdP), including
203 the assumed slip system, based on the methodology of Thomas et al. (2011). These models
204 were constructed by assuming horizontal simple shear at the base of the mantle, where the
205 dominant slip direction aligns parallel to the CMB, the slip plane is assumed to be

206 horizontal, and 12% of the aligned single crystals are mixed linearly with its isotropic
207 equivalent. This choice of 12% alignment was based on the previous work of Thomas et
208 al. (2011), and yields reasonable anisotropic strengths; since we focus on reflection
209 polarities and not amplitudes, however, this choice of value is not critical. We assume that
210 the aligned grains are sub-parallel with the slip direction and the slip plane is sub-parallel
211 to the CMB and the remaining grains are randomly oriented for Models A, B, and C (Figure
212 3). We tested three models (Models A [Ppv], C [Br], and D [Fp] in Table 2) in which the
213 D" discontinuity represents a change in alignment of the mineral grains from an isotropic
214 (above the discontinuity) to an anisotropic (below the discontinuity) regime. In Model B,
215 the D" discontinuity is an isotropic phase transformation from Br to anisotropic Ppv. The
216 predicted values for reflection polarities for each model are shown in Figure 3 and were
217 calculated using Guest and Kendall (1993) from the velocity perturbation and reflection
218 coefficients at the interface between an isotropic and anisotropic layer with respect to
219 azimuth from the dominant slip direction and epicentral distance (Thomas et al., 2011).

220 Our approach to calculating predicted shear wave splitting parameters and
221 reflection polarities for our synthetic models makes several simplifying assumptions. First,
222 we only directly model shear wave splitting due to lowermost mantle anisotropy, and
223 ignore any potential contributions from the upper mantle. Our approach therefore assumes
224 that any upper mantle contribution (in real data) has been correctly accounted for; we
225 further assume that the bulk of the lower mantle is isotropic (Meade et al., 1995). We do
226 not explicitly consider how incorrect upper mantle corrections could bias the resulting D"
227 observations, which is beyond the scope of our study. Second, we rely on ray theory and
228 do not consider finite frequency wave effects in our modeling. Ray theoretical predictions

229 are generally adequate for homogenous regions of D'' (e.g., Nowacki and Wookey, 2016),
230 although they may break down for laterally heterogeneous anisotropic models
231 (heterogeneities varying over hundreds of km). Third, in our modeling we approximate the
232 propagation directions for SKS and SKKS with average inclination angles for these phases,
233 and for ScS we assume that propagation is horizontal through the D'' layer. This assumption
234 follows previous work (Nowacki et al., 2010; Ford et al., 2015; Creasy et al., 2017). In the
235 Earth and at the relevant epicentral distances, ScS can be inclined from the horizontal up
236 to $\sim 15^\circ$, but this assumption has only a modest effect on the predicted splitting parameters.
237 We assume the three different phases (SKS, SKKS, and ScS) propagate at different
238 inclination angles: $\sim 55^\circ$, 35° , 0° from the horizontal, respectively. Inclination angles are
239 based on a straight-line approximation, calculated using TauP (Crotwell et al., 1999) based
240 on the PREM Earth model (Dziewonski and Anderson, 1980) for distances of $90^\circ - 120^\circ$
241 for SKS/SKKS and $60^\circ - 80^\circ$ for ScS with an event at a depth 10 km. We use these average
242 propagation angles for SKS and SKKS in our modeling for simplicity, although for real
243 data they can vary by 10° to 20° from these average values.

244

245 2.3 Modeling approach and strategy

246 Our goal is to conduct a series of stochastic forward modeling simulations to test
247 whether we can uniquely constrain a given starting model (an elastic tensor) and its
248 orientation using a dataset with a given set of characteristics (e.g., number and type of
249 measurements, azimuthal distribution). Our forward modeling framework follows Ford et
250 al. (2015), who modeled a shear wave splitting dataset that samples the lowermost mantle
251 beneath the Afar peninsula along the edge of the African LLSVP. We did not consider

252 delay times in our modeling. Individual delay time measurements contain larger error bars,
253 which limit the utility of using the relative travel times in a dataset as a discriminant. The
254 complete tradeoff between fabric strength and layer thickness also limits the utility of using
255 absolute travel times as a constraint.

256 For each of our modeling experiments, we first choose a starting model and
257 orientation from the possibilities listed in Table 1. As an example, we first consider a
258 horizontally aligned elastic tensor of Ppv with [100] and [010] axes parallel to the CMB,
259 which we will use to illustrate our approach in several of the following figures. Second, we
260 randomly identify a set of raypaths of SKS, SKKS, and/or ScS sometimes in combination
261 with SdS and PdP reflection polarities. Third, we calculate the predicted fast-axis directions
262 and/or reflection polarities of SdS and PdP for each raypath, as described in Section 2.2.

263 In the fourth step, we model the synthetic dataset by applying the same forward
264 modeling technique that we typically use for real data (Ford et al., 2015). Specifically, we
265 treat the synthetic observations as though the actual model used to generate them was not
266 known, and test all possible models listed in Tables 1 and 2 in all possible orientations
267 (every 5°) to identify models/orientations that are consistent with the synthetic dataset. A
268 candidate model/orientation is discarded if the predicted and “observed” fast splitting
269 directions differ by more than 20° or if the predicted reflection polarities are opposite to
270 those of the “observations”. We apply this 20° cutoff for the splitting observations, based
271 on methods and reasonable estimates of errors in previous shear wave splitting studies (see
272 Ford et al., 2015). While this misfit criterion is appropriate for measurement errors, it does
273 not take into account effects such as inaccurate upper mantle corrections for actual D”
274 anisotropy observations or the possible finite-frequency effects of complex structure.

275 Explicit consideration of these effects in D” anisotropy studies is a subject of ongoing
276 research. For each candidate model/orientation that was considered an acceptable fit to the
277 synthetic data, we calculated a total misfit value for the fast polarization directions only
278 based on a residual sum of squares approach, following Ford et al. (2015). Each fast
279 direction misfit is normalized by the maximum residual of 90° and summed by using the
280 residual sum of squares, in which we calculate the square of the difference between the
281 observation and data prediction.

282 The fifth and final step in our modeling strategy is to repeat the entire process a
283 large number (M) of times for random raypath configurations. All of these steps are
284 illustrated in Figure 4. In each iteration, we randomly choose a new azimuthal distribution
285 of raypaths for a new synthetic dataset with varying characteristics (such as the number
286 and type of observations, described in more detail below). We report our results by
287 considering what percentage of the M iterations could uniquely identify the starting model.
288 Each individual iteration was designated as “*uniquely constrained*” if it successfully
289 identified the correct starting model and could completely rule out any other candidate
290 model. However, if there was at least one other anisotropy configuration (any candidate
291 elastic tensor model, in any orientation) which was found to be consistent with the synthetic
292 observations, then that iteration was designated “*not uniquely constrained.*” Therefore, all
293 our model results are characterized through a %-*uniquely constrained* value, which
294 identifies what percentage of the M simulations could uniquely constrain the starting
295 model. The actual values of these “%-uniquely constrained” estimates are strongly
296 dependent on our modeling choices, and the estimates could change with different

297 modeling assumptions. However, these percentages can be compared across our suite of
298 numerical simulations, since our assumptions are consistent across the various tests.

299 Within this modeling framework, we tested a series of synthetic dataset
300 characteristics described by the following three distinct variables: the number of
301 measurements (N), ratio of the number of SK(K)S (that is, SKS plus SKKS) measurements
302 to the total number of shear wave splitting measurements (we term this ratio the “SKS
303 number”), and the azimuthal distribution of measurements, as quantified by the angular
304 dispersion (R). Angular dispersion is defined as:

$$305 \quad C_P = \sum_{i=1}^n \cos(a_i), \quad S_P = \sum_{i=1}^n \sin(a_i), \quad (1)$$

$$306 \quad R = \sqrt{C_P^2 + S_P^2}, \quad (2)$$

307 where a_i is a vector of directions and R is angular dispersion, which varies from 0
308 (uniform dispersion) to 1 (concentration in one direction) (Mardia and Jupp, 2000). A
309 graphical definition of R is shown in Supplementary Figure S1.

310 We tested different combinations of N and SKS number to gain insight into how
311 many measurements, and in what combination, are typically needed to uniquely constrain
312 the anisotropy. For angular dispersion, we calculated the value of R for each of the M
313 iterations carried out in each test; then, we queried the large number of simulations to
314 understand how the azimuthal distribution of the synthetic data affected its ability to
315 constrain anisotropy.

316

317 2.4 Distinguishing the mechanism and orientation of anisotropy

318 For the first round of tests, we sought to understand how many shear wave splitting
319 measurements, and in what combination (as described by the SKS number), are generally

320 needed to uniquely constrain the *mechanism* for anisotropy. That is, we tested whether
321 synthetic datasets could be shown to be consistent *only* with the correct starting model (e.g.,
322 Ppv, as opposed to other models listed in Table 1), and with *no other* candidate mechanism.
323 For this round of tests, we used the single crystal models in Table 1 as starting models,
324 each in several different orientations. The LPO model of Ppv was only used for the second
325 round of tests. We defined the starting model orientation via the rotation angle about the
326 [100] axis from the horizontal (note that Figure 2 only shows an example with a horizontal
327 [100] and [010] direction). We arbitrarily tested each single crystal model at three different
328 orientations based on the rotation angle about the [100] axis from the horizontal: 0°, 45°,
329 and 90°. For the LPO model of Ppv, we only test the original orientation for the starting
330 model and do not test a rotated version of the elastic tensor since this model is based on a
331 region in the Walker et al. (2011) with horizontal shear. In our initial round of tests, we
332 focused only on cases in which shear wave splitting observations of SKS, SKKS, and ScS
333 (for varying N, SKS number, and R values) were used to constrain the models. In later
334 tests, we explored scenarios in which reflection measurements were combined with shear
335 wave splitting data in order to estimate the improvement obtained by combining different
336 data types.

337 We also carried out a series of tests whose goal was to constrain the *orientation* of
338 the elastic tensor for the case in which the mechanism for anisotropy is known (or
339 assumed). For this line of inquiry, we focused on Ppv as a test case; we did not test other
340 mechanisms in this part of the study. The choice to focus on Ppv was made for simplicity
341 and because Ppv is often invoked as the preferred mechanisms for anisotropy in D" (Creasy
342 et al., 2017; Ford et al., 2015; Ford and Long, 2015; Nowacki et al., 2010; Thomas et al.,

343 2011a; Wookey et al., 2005b). We consider both single-crystal Ppv tensors and elastic
344 tensors derived from texture modeling, as discussed above. As in our first series of tests,
345 we initially focus on synthetic datasets that only contain shear wave splitting observations,
346 and then examine cases that also include reflection measurements.

347 Lastly, in addition to the two major lines of inquiry we address in our modeling
348 (what kind of datasets are needed to constrain the *mechanism* and *orientation*) of lowermost
349 mantle anisotropy, we performed two practical tests using horizontal Ppv as a starting
350 model. First, we carried out a test of how many iterations (that is, values of M) are needed
351 for our forward algorithm to converge on an estimate of the probability of identifying
352 unique models. Second, we tested the addition of Gaussian noise to the shear wave splitting
353 predictions, in order to understand how well real, noisy datasets might perform. The results
354 of these practical tests are described below. While seismic data can deviate from a Gaussian
355 distribution (Groos and Ritter, 2009), we only consider Gaussian distributed noise here
356 since in an ideal case, seismic noise is Gaussian distributed (Bendat and Piersol, 2011).

357

358 **3. Results**

359 3.1 Illustrative examples: Model runs for a ppv starting model

360 To illustrate the process and results of our modeling, we discuss here the results
361 from a test that attempts to constrain the *starting model*, as well as one iteration of a test
362 that attempts to constrain the *orientation*. In both cases, we use synthetic shear wave
363 splitting data only. For these examples, as in all of our tests, we follow the five steps of our
364 method outlined above (Figure 4): (1) choose a starting model and orientation, (2) choose
365 the number of observations and the SKS number to randomly generate a distribution of

366 raypaths, (3) calculate the predicted fast polarization directions (of SKS, SKKS, and ScS)
367 and reflection polarities (for SdS and PdP) for the synthetic dataset for the chosen starting
368 model, (4) conduct a forward modeling search over all possible orientations for all possible
369 candidate models to eliminate all models/orientations that do not fit the “observations”
370 using a misfit cutoff. Then, if all other models and orientations can be eliminated by
371 applying the misfit cutoff, this set of synthetic raypaths are able to uniquely constrain the
372 starting model and designated as “*uniquely constrained.*” The fifth step would be repeating
373 this process M number of times but for this illustrative example, $M = 1$.

374 Our illustrative example is shown in Figure 5. For this example, we chose a starting
375 model of non-rotated Ppv (in this case, the [100] and [010] crystallographic axes are
376 parallel to the CMB) (Figure 5a). In all of our single-crystal elasticity tests, we do not
377 assume a dominant slip system; rather, we invoke a starting orientation in the geographic
378 reference frame identified by the angle of the mineralogical axes. This particular example
379 involves 9 splitting observations, 6 of which are SK(K)S (that is, an SKS number of 2/3).
380 The randomly generated azimuthal distribution of these chosen phases is shown in Figure
381 5b. The predicted fast polarization directions for our chosen model and ray configuration,
382 plotted in a ray-centered reference frame, are shown in Figure 5c. A search over all possible
383 candidate models and orientations (rotating every 5°) shows that there is no other model,
384 other than the correct starting model (Ppv), that can match each of the synthetic fast
385 splitting directions to within 20° (our pre-defined misfit cutoff). Put another way, for every
386 possible combination of starting model and orientation (other than the correct, known
387 starting model), at least one predicted fast splitting orientation differed from that in the
388 dataset by more than the 20° misfit cutoff. Since this particular configuration of

389 observations could uniquely identify the starting model and no other models, it is
390 designated “*uniquely constrained*.”

391 This particular example illustrates a single iteration ($M = 1$) of our testing, but the
392 power of our approach lies in repeating this a large number of times to understand what
393 percentage of randomly generated synthetic datasets have the ability to uniquely constrain
394 the starting model. In order to understand how many iterations are needed to converge on
395 an estimate of this probability, we conducted an “iteration test” for our horizontal Ppv
396 starting model, as shown in Figure 6. For this test, we used 9 shear wave splitting
397 measurements ($N = 9$) and an SKS number of $2/3$, as in the example shown in Figure 5,
398 and ran a large number of iterations ($M = 50,000$), each involving a new, random
399 distribution of propagation azimuths. After each successive iteration, we calculated the
400 percentage (of M iterations) for which the synthetic dataset was able to *uniquely constrain*
401 the starting model, as shown in Figure 6. For this starting model, after a large number of
402 iterations, we found that 41% of all iterations could uniquely constrain the starting model,
403 while for the other 59% of the raypath configurations, there was another model/orientation
404 that could simulate the synthetic data. Our running estimate of how likely a dataset with 9
405 splitting observations (6 SK(K)S, 3 ScS) converges on an average value of 41% after
406 approximately 1,000 iterations (Figure 5). Based on this iteration test, we have chosen to
407 run each of our numerical experiments for $M = 5,000$ iterations, balancing computational
408 cost and the need for our estimates to converge.

409 Next, to illustrate our process for testing whether synthetic data can identify a
410 unique starting *orientation*, we show in Figure 6 two examples of searching for the correct
411 starting orientation for the same horizontal Ppv starting model as in Figure 4. For this

412 example, we chose two different raypath configurations, one with $N = 8$ observations (5
413 SKS+SKKS and 3 ScS; Figure 7a) and one with $N = 4$ (3 SKS+SKKS and 1 ScS; Figure
414 7b). We assume that the mechanism for anisotropy is known to be Ppv and that the elastic
415 constants are known, and search over all possible orientations to test whether there are
416 additional configurations (other than the known starting orientation) that can reproduce the
417 synthetic observations.

418 Figures 7a and 7b show all possible orientations that satisfy this suitability criterion
419 for each of our two examples ($N = 8$ and $N = 4$, respectively), with each orientation color-
420 coded by its calculated misfit value (Equation 1). Following Ford et al. (2015), we search
421 for local minima of misfit within the 3-D rotation space. For our $N = 8$ case (Figure 7a),
422 the set of 8 measurements could uniquely identify the starting orientation, and would be
423 designated as “uniquely constrained.” However, for our $N = 4$ case (Figure 7b), we
424 identified two other possible orientations (that is, the known correct starting orientation,
425 plus two others). Therefore, for this particular raypath configuration, the solution is
426 designated “not uniquely constrained.” We note, however, that the orientation with the
427 lowest misfit value (magenta dot in Figure 7b) is, in fact, the correct starting orientation.

428 Finally, we illustrate an example calculation that includes Gaussian noise in the
429 synthetic observations (Figure 7c). This test relies on the same horizontal Ppv starting
430 model, and uses the same raypath configuration ($N = 4$) as the test shown in Figure 7b. The
431 only difference is that when the predicted shear wave splitting fast directions are calculated
432 based on the starting model and raypath distribution, we add Gaussian noise to the fast
433 splitting direction “observations,” with a maximum error excursion of 20° and a standard
434 deviation of 9° . Figure 7c reveals that the case with Gaussian noise produced the same two

435 possible sets orientations as fitting the data, but now the solution with the minimum misfit
436 is not associated with the correct solution.

437

438 3.2 Results: Constraining the anisotropy mechanism

439 Building on the illustrative examples discussed in section 3.1, we now explore the
440 results of a large number of simulations with different starting models and raypath
441 configurations. We first address the question of what kind of datasets are needed to
442 distinguish among the various models listed in Figures 2 and 3. For this suite of numerical
443 experiments, we examined a variety of starting models and orientations, as well as a variety
444 of raypath configurations (as defined by the number of splitting measurements, the SKS
445 number, and the angular dispersion of the raypath azimuths). The results of these
446 experiments are shown in Figure 8. We first examine those model runs that only included
447 shear wave splitting data, shown in the nine panels of Figure 8a.

448 We initially focus on the mechanism and orientation of the starting model (Figure
449 8a, left panels), and explore how the probability of uniquely constraining the mechanism
450 varies as a function of the number of measurements. For each of the models considered,
451 the probability of identifying the unique starting model increases with the number of
452 measurements as expected. Typically, there is a sharp increase in the probability for N
453 values between six and nine measurements. In all cases, approximately 9 measurements
454 are needed in order to have a ~50% chance of constraining the starting model, while a high
455 number of splitting measurements ($N \approx 15$) is needed for the probability to reach ~90%.
456 For comparison, the datasets of Ford et al. (2015) and Creasy et al. (2017) contained

457 between four and eight splitting measurements. The starting model with the highest success
458 rate at constraining the mechanism is Br, as opposed to Fp and Ppv.

459 The probability of constraining the starting mechanism depends on the orientation
460 of the starting model; as shown in Figure 8a, we tested orientations with a horizontal [100]
461 crystallographic axis, 45° rotated about the [100], and 90° rotated about the [100] axis.
462 Interestingly, for Ppv it is easier to uniquely constrain the starting model in the 90° case;
463 in contrast, for Br the chances are highest for the horizontal case, and for Fp the chances
464 are substantially higher for the tilted case. The reason for this result for Ppv can be
465 discerned by examining the predicted splitting patterns in Figure 2. For the horizontal case,
466 predicted fast splitting directions for ScS do not vary with azimuth; however, if the Ppv
467 tensor is rotated by 90° about the [100] axis, there is significant variation in fast directions
468 with azimuth. With greater variability in the predicted fast polarization directions (lower
469 angular dispersion), there is a higher probability of constraining that model for a given
470 number of ScS observations. A similar principle is at work for Fp: ScS fast directions do
471 not vary with azimuth for either horizontally or vertically aligned Fp, but in the tilted case,
472 variability is present. Generally, the anisotropy scenarios that yield higher chances of
473 uniquely constraining the starting model have lower mean angular dispersion values of the
474 predicted fast-axis directions (Supplementary Figure S2). Models that have little variation
475 in fast-axis directions with azimuth, such as non-rotated Fp, are more difficult to uniquely
476 constrain (Figure S2c and Figure 8a).

477 We also examined how the balance between SKS+SKKS vs. ScS phases in the
478 synthetic dataset affected the ability of the synthetic “observations” to uniquely constrain
479 the starting model (Figure 8a, middle panels). For these experiments, we varied the SKS

480 number from 0 (all ScS measurements) to 1 (all SKS+SKKS measurements) for a fixed
481 value of $N = 9$. For very high or low values of SKS number we find a low probability of
482 uniquely constraining the starting model with substantially higher probabilities for
483 intermediate SKS numbers. The optimal ratio of SK(K)S phases to total measurements
484 differs slightly for different starting models, but in general an SKS number between 0.5
485 and 0.8 maximizes the chances of constraining the anisotropic mechanism. In all cases, a
486 combination of ScS and SK(K)S shear wave splitting observations, instead of splitting
487 measurements for just one phase type, will drastically improve the probability of
488 constraining the starting model.

489 Additionally, we explored the importance of how the angular distribution of the
490 synthetic raypaths affected the ability to constrain the starting model, finding only a weak
491 effect (Figure 8a, right panels). As expected, datasets with a wide angular distribution (R
492 < 0.2) have the largest probability of uniquely constraining the starting model in all cases.
493 At very large values of angular dispersion ($R > 0.8$), for which the raypaths are clustered
494 over a narrow range of azimuths, the splitting “observations” are sampling similar parts of
495 the elastic tensor. Because of this, datasets that are tightly clustered in azimuth cannot
496 capture the symmetry of the tensor and cannot distinguish among different candidate
497 mechanisms for anisotropy. For intermediate values of R , the dependence on R is not
498 strong.

499 Finally, we explored the value of combining shear wave splitting and reflection
500 polarity measurements when trying to uniquely constrain an anisotropic model. Figure 8b
501 shows the results of adding a single reflection polarity measurement (that is, a measurement
502 of PdP and SdS polarities for a single raypath) to a dataset of shear wave splitting

503 measurements. For this test, we considered a smaller number (four) of potential candidate
504 models (as shown in Figure 3), so the probabilities of uniquely constraining the anisotropy
505 mechanism are generally higher than in our other tests. For this test, we chose a raypath
506 configuration involving an SKS number of 0.67 and varied the number of shear wave
507 splitting measurements from 0 to 15. We used a starting model A in Figure 3 (anisotropy
508 due to Ppv), and tested configurations that involved both shear wave splitting
509 measurements and one additional set of reflection polarity measurements (both PdP and
510 SdS) at a single azimuth. This test (Figure 8b) demonstrates that despite the fact that
511 reflectivity measurements provide only binary information (positive or negative polarities),
512 the incorporation of a different data type into the test increases the probability of uniquely
513 constraining the starting model. In some cases, this increase is substantial; specifically, for
514 datasets containing between four and eight shear wave splitting measurements. The
515 addition of reflection polarity data can increase the probability of constraining the starting
516 model by ~10-18% (right panel of Figure 8b).

517

518 3.3 Results: Constraining the anisotropy orientation

519 The tests shown in Figure 8 illustrate the ability of shear wave splitting and
520 reflection polarity data to constrain the anisotropic mechanism if the algorithm is allowed
521 to consider a range of possible models. We now turn our attention to tests in which we
522 assume that the mechanism that creates the anisotropy, as well as the elastic constants
523 associated with that mechanism, are known, but the orientation of the elastic tensor is not
524 known. In general, this is an easier problem than uniquely constraining the starting model,
525 as the observations need not distinguish among different candidate elastic tensors, only

526 among different possible orientations. In practical terms, this type of modeling exercise
527 would be suitable for datasets that sample a region of the lowermost mantle whose
528 mineralogy and temperature conditions can be constrained using independent observations
529 or models (for example, seismic velocities in combination with mineral physics
530 constraints).

531 For this set of tests, we first consider single-crystal Ppv in three different
532 configurations: 1) [100] and [010] axes oriented in the horizontal plane, 2) a 90° rotation
533 about the [100] axis, and 3) randomly chosen orientations. For the third configuration, we
534 randomly identified nine different, unique starting orientations. These randomly generated
535 orientations were used for each of the ~5,000 iterations in this scenario. As with the tests
536 discussed in section 3.2, we tested a variety of raypath configurations with a range of N
537 (number of measurements), SKS number, and examined how our results varied with the
538 angular dispersion characteristics of the synthetic raypaths. The results of our single-crystal
539 Ppv tests are shown in the top row of Figure 9. The results for our collection of nine random
540 starting orientations are shown in detail in Supplementary Figure S3.

541 As expected, our tests demonstrate that uniquely constraining the orientation of the
542 starting model is much easier and requires fewer measurements than uniquely constraining
543 the starting model/mechanism (Figure 7). In general, a ~50% probability of correctly
544 retrieving the anisotropy is achieved with as few as six to nine splitting measurements (top
545 left panel of Figure 9a). The orientation of the starting model does affect the likelihood of
546 uniquely identifying the anisotropy orientation. With our randomly generated starting
547 orientations, the probability of constraining the starting orientation varies (Figure S3), but
548 on average randomly oriented starting models do slightly worse compared to the results

549 shown in Figure 9. For nine measurements, the randomly orientated models on average
550 find the correct orientation in 65% of all simulations, compared to Figure 9, where a non-
551 rotated and Ppv rotated by 90° can constrain on average 75% of the simulations. As with
552 our previous tests, it is clear that a mixture of SK(K)S and ScS shear wave splitting
553 measurements provide the highest likelihood of constraining the starting orientation,
554 although the optimal mix of ScS and SK(K)S depends on the starting model orientation.
555 Our tests confirm that datasets that contain only ScS measurements (that is, SKS number
556 of zero) cannot constrain the azimuth of the Ppv elastic tensor if its [100] axis is horizontal,
557 due to the lack of variability in predicted fast polarization direction (Figure 2). The
558 dependence of our results on angular dispersion of the propagation azimuths (right panels
559 of Figure 9a) are similar to those for the case in which we attempted to retrieve the starting
560 model; in general, a wide distribution of azimuths will increase the probability of uniquely
561 constraining the orientation of Ppv, while datasets whose propagation azimuths are tightly
562 clustered are less ideal. The same is generally true for the random starting models, despite
563 some small excursions from the overall trend (Figure S3). These small excursions or
564 “bumps” in the curves are artifacts, and are related to stochastic variations in the
565 distribution of the predicted fast splitting directions for different models.

566 Next, we considered elasticity models that explicitly take into account texture
567 development in a polycrystalline aggregate, in addition to the single-crystal elastic tensors
568 that are the main focus of our study. While there are many uncertainties in texture models
569 for Ppv at lowermost mantle conditions, these models may be more representative of a
570 realistic texture of aligned Ppv mineral grains. We only considered one case, invoking
571 dominant slip on the (010) plane. Somewhat surprisingly, we found that for modeled Ppv

572 LPO, there is a much lower probability of constraining the orientation of the elastic tensor
573 than for test cases that used a single crystal elastic tensor (Figure 8a). We investigated
574 possible reasons for this, and found that in contrast to the single-crystal models, for the
575 textured Ppv model it is fairly common for the algorithm to identify what we term as
576 “unstable” solutions, which are illustrated in Figure S4. In this situation, a certain
577 orientation might fit the observations, but adjacent orientations (in which the elastic tensor
578 is rotated by 5°) do not. This is in contrast to the behavior of single-crystal elastic models
579 (Figure 2), in which the best-fitting orientations are adjacent to other solutions that also fit
580 the data (in other words, the misfit values vary smoothly as a function of rotation angles of
581 the candidate tensors). In addition, the presence of unstable solutions is highly dependent
582 on our use of the misfit criterion of 20° . Figure S4 shows results for a range of misfit cutoff
583 values, and demonstrates that these unstable solutions disappear with the application of
584 more conservative misfit criteria.

585 We define a “stable” solution as one in which, if the elastic tensor is rotated slightly
586 ($\sim 5^\circ$ in any direction), the rotated elastic tensor would still yield an acceptable fit to the
587 synthetic data. In contrast, an “unstable” solution is one that has no adjacent orientations
588 that yield an acceptable fit to the data. For the case of the textured Ppv model, the algorithm
589 generally identifies many “unstable” orientations (Figure 9); again, this is in contrast to the
590 generally “stable” orientations identified for single-crystal Ppv (Figure 7). In order to
591 illustrate the effects of these unstable solutions, we applied a sensitivity cutoff to our
592 textured Ppv simulations (Figure 8a, second row) to illustrate the effects of removing all
593 unstable solutions. If we consider only stable solutions, the probability of uniquely
594 constraining the starting orientation increases by 20% on average (Figure 9a).

595 In order to identify the starting orientation of the Ppv LPO, we found that a mixture
596 of SK(K)S and ScS shear wave splitting measurements again provide the highest likelihood
597 of constraining the orientation (Figure 8a: bottom, middle panel). There is a clear
598 dependence on angular dispersion (Figure 9a: bottom, right panel). Specifically, with low
599 values of R (0-0.1) and middle values of R (0.5-0.7), there is a higher probability of
600 constraining the orientation, while there is a decrease in probability between $R = 0.1$ and
601 $R = 0.4$. In all other cases and starting models, we have not observed this pattern of
602 dependence with R . While there is no explanation for this pattern, large values of R (0.8-
603 1.0) resulting in low probabilities of finding the starting orientation is consistent with all
604 other tests.

605 Returning to our consideration of single-crystal Ppv models, and as in section 3.2,
606 we considered the effect of adding a reflection measurement to shear wave splitting
607 observations to constrain the orientation of the single-crystal Ppv starting model (Figure
608 9b). For this test, we used a starting model that invokes an isotropic ppv layer over an
609 anisotropic ppv layer with dominant [100](010) slip (Model A in Figure 3). As in the
610 previous test, we find that just adding one observation of reflection polarity measurements
611 improves the probability of constraining the starting orientation (Figure 9b), although the
612 improvement was somewhat less dramatic. Again as with the previous tests, the relative
613 improvement is greatest for datasets with number of measurements N roughly between 5
614 and 9.

615 Finally, in a test analogous to the Gaussian noise test discussed in section 3.1 and
616 illustrated in Figure 7c, we considered a single-crystal Ppv test in which we tried to retrieve
617 the correct starting orientation using synthetic observations that included random, Gaussian

618 distributed errors on the fast polarization predictions (Figure 10). We found that adding
619 Gaussian noise to the fast polarization directions, normally distributed between -20° and
620 20° with a mean of 0° and standard deviation of 9° , does not significantly hinder the
621 probability of constraining the starting model's orientation (Figure 10a). However, this test
622 allowed us to explore the distinction between *uniquely* constraining the starting model's
623 orientation and identifying a model with a *minimum* misfit value that corresponds to the
624 correct starting orientation. For the error-free synthetic datasets, the minimum misfit value
625 always corresponds to the correct orientation, even for cases in which other orientations
626 are allowed by the data. For cases where Gaussian error is incorporated into the synthetic
627 dataset, the synthetic dataset may result in an incorrect solution, where the minimum misfit
628 value may be different from the correct solution. This observation led us to carry out a test
629 (Figure 10b) in which rather than attempting to *uniquely* constrain the correct starting
630 orientation, we tested whether the best-fitting orientation (that is, the candidate orientation
631 with the minimum misfit value) actually corresponded to the correct starting orientation.
632 We further tested whether the best-fitting solution in terms of misfit was oriented within
633 10° - 20° of the known, correct starting orientation. Encouragingly, we found that the
634 probability that the minimum misfit solution was within 20° of the correct orientation
635 exceeded 50% for datasets with a relatively small number of shear wave splitting
636 measurements ($N \approx 4$).

637

638 **4. Discussion**

639 4.1 Implications for the interpretation of real-world data sets

640 Understanding the scope of information about lowermost mantle anisotropy
641 contained in shear wave splitting and reflection polarity observations is crucial for our
642 ability to relate anisotropy observations to flow at the base of the mantle. While the
643 mechanisms of lowermost mantle anisotropy remain imperfectly known, the results
644 presented in this paper reveal observational strategies that can maximize the probability of
645 constraining the mechanism and/or orientation, regardless of the actual anisotropic
646 geometries present. This work shows that a diversity of shear wave splitting measurements
647 and reflection polarity data is essential, and the modeling of single phases (e.g., ScS, SKS,
648 SdS) is typically insufficient to constrain anisotropic geometry.

649 Specifically, this work demonstrates that because different seismic phases (ScS,
650 SKS, SKKS, PdP, SdS) propagate through or reflect off the D" region at different angles
651 from the horizontal, a combination of these phases is more useful for constraining
652 anisotropy than datasets with wide azimuthal coverage. Consider, for example, a
653 hypothetical case in which 9 unique splitting measurements for ScS phases are used to
654 probe an anisotropic structure consisting of horizontal, single crystal post-perovskite. In
655 this case, post-perovskite can only be distinguished from other plausible anisotropic
656 models less than 10% of the time (Figure 8a and 9a). However, if SK(K)S phases and/or
657 reflection polarities are incorporated into the analysis, then we can distinguish between the
658 two possible mechanisms nearly 40% of the time (Figure 8a). In all cases of varying starting
659 models and orientations, a combination of different types of data increases the probability
660 of constraining the starting model by 10% to 60%. This pattern also generally holds true
661 for finding the orientation of the Ppv elastic tensor. A diversity of data increases the
662 likelihood of constraining the orientation of Ppv anisotropy anywhere from 10% to 50%

663 for 6 unique measurements. Interestingly, we observed an exception to this (Figure 9a) for
664 Ppv oriented at an azimuth of 90° , where only ScS splitting data (SKS number of 0) had
665 the best chance to constrain the starting orientation.

666 Body wave datasets that probe seismic anisotropy in the lowermost mantle should
667 combine both multiple data types and wide azimuthal coverage to maximize the probability
668 that the anisotropic geometry can be tightly constrained. Figure 11 illustrates regions in the
669 mantle in which all of the body wave measurement methods could potentially be applied
670 simultaneously. This map was generated by considering the actual distribution of high-
671 magnitude ($M > 6.5$) seismicity on Earth, in combination with a database of long-running
672 broadband seismic stations beneath which the upper mantle anisotropy pattern has been
673 shown to be simple enough to correct for (Lynner and Long, 2013, 2014b). While there are
674 many regions of D'' with limited raypath coverage for the types of data considered in this
675 study, we find that North America, the Arctic, northwestern Pacific, and Australia are
676 regions that represent ideal targets to collect a diverse set of observations to further
677 constrain D'' anisotropy.

678 Our results inform our view of why previous studies that included crossing raypaths
679 (e.g., Ford et al., 2015; Creasy et al., 2017) were unable to uniquely constrain a model for
680 D'' anisotropy. Our study indicates that a relatively large number of shear wave splitting
681 measurements (approximately 9 or more for most cases in Figure 8a) are needed to have at
682 least a 40% to 60% chance of uniquely identifying the starting model. The observational
683 datasets of Ford et al. (2015) and Creasy et al. (2017) included approximately four to eight
684 shear wave splitting measurements over unique azimuths in the lowermost mantle (Table
685 3). The synthetic models presented in this paper help to provide context for why these

686 studies have not been able to uniquely constrain a particular mechanism or orientation for
687 anisotropy (e.g. Ford et al., 2015, Creasy et al., 2017). For example, each of these studies
688 (Table 3) had relatively high angular dispersion values for their range of predicted fast
689 splitting directions (greater than 0.4 in all cases). As discussed in section 3.2, datasets with
690 lower angular dispersion values are generally more successful at constraining a unique
691 elastic tensor. Therefore, even though many of the studies listed in Table 3 used diverse
692 data types with combinations of SKS, SKKS, and ScS, they could not uniquely constrain
693 an anisotropy mechanism or orientation when testing the elastic tensors considered in this
694 study. The studies that used one type of observation (Nowacki et al., 2010; Thomas et al.,
695 2011) did not consider all possible elastic tensors and orientations that we tested here, so
696 we cannot directly compare them with the results of our synthetic tests. If the mechanisms
697 for anisotropy and the associated elastic tensors can be reliably assumed, there is generally
698 a higher chance of identifying the correct orientation and inferring the correct mantle flow
699 geometry. With only 9 measurements, there is a 40% to 80% chance of uniquely
700 constraining the orientation of post-perovskite (Figure 9a), an improvement from the
701 chance of uniquely identifying the elastic tensor itself (a 40%-60% chance). Consideration
702 of these results in future studies of D'' anisotropy, as well as a more detailed consideration
703 of how errors and uncertainties propagate in forward models, should enhance our ability to
704 characterize anisotropy at the base of the mantle. A more detailed statistical analysis may
705 be required similar to this study to fully explore the error and model space.

706

707 4.2 Practical considerations

708 Our tests that assumed Gaussian error on the predicted fast splitting directions
709 (Figure 10b) demonstrate that it does not significantly affect the probability of constraining
710 the model, as compared to noise-free synthetic data. When including Gaussian error, we
711 found that as few as four shear wave splitting measurements can identify the correct
712 orientation within 20° more than 50% of the time. Datasets of this size (roughly four unique
713 measurements in the same region of D”) can likely be reasonably achieved in many regions
714 of the lowermost mantle, based on the distribution of available raypaths (Figure 11). This
715 finding may help with the interpretation of modeling results for real splitting datasets, such
716 as those considered by Ford et al. (2015) and Creasy et al. (2017), for which multiple
717 possible anisotropic orientations were identified, but particular orientations had
718 significantly lower misfit values than others.

719 Our synthetic modeling results also shed light on potential complications in
720 interpretation caused by the different symmetry classes of some of the candidate elasticity
721 scenarios that have been proposed to explain lowermost mantle anisotropy. To effectively
722 differentiate these scenarios using shear wave splitting data alone, it is crucial for splitting
723 datasets to probe the symmetry of the mineral such that no other elastic tensor simulates
724 that pattern for a similar range of propagation directions. Of the candidate scenarios we
725 tested in this study, Fp has the highest (cubic) symmetry with only 3 unique constants in
726 the elastic tensor. SPO models have the next highest symmetry, since tubule and oblate
727 SPO models are hexagonal (transversely isotropic) with 5 unique elastic constants. Ppv and
728 Br are both orthorhombic, with the same order of symmetry and only 9 unique elastic
729 constants. In more complicated models, such as LPO calculations of single crystals, the
730 symmetry is much lower than its single crystal counterpart with 21 unique elastic constants.

731

732 4.3 Limitations of our modeling approach

733 We caution that our synthetic tests must be interpreted in light of the still-
734 considerable limitations in our understanding of the elasticity of anisotropic materials at
735 lowermost mantle conditions. We have focused mainly on single-crystal elastic tensors,
736 derived mainly from ab initio simulations, as a reasonable starting point in this study;
737 however, predictions of single-crystal elasticity are likely imperfect and do not take into
738 account effects such as variation in composition. Furthermore, single-crystal elasticity is
739 an imperfect proxy for the likely anisotropic geometry of polycrystalline aggregates,
740 particularly for minerals with high symmetry such as Fp (e.g., Yamazaki and Karato,
741 2002). The further consideration of elasticity models that explicitly take into account
742 texture development will be an important step, although texture models include a number
743 of poorly known parameters (such as activation energies for different slip systems) and
744 consensus on the dominant slip systems in different lowermost mantle minerals remains
745 elusive (e.g., Nowacki et al., 2011).

746 Another limitation of the work proposed here is that it is carried out in the context
747 of ray theoretical predictions, assuming infinite frequency, rather than considering the full
748 characteristics of the waveform at finite frequencies. With improvements on both
749 observational and modeling techniques that model the full waveform (e.g., Kawai and
750 Geller, 2010, Nowacki and Wookey, 2016, Parisi et al., 2018), the interpretation of seismic
751 anisotropy observations can very likely be improved. In particular, future work must
752 investigate how the measurement techniques used influence the interpretation of finite
753 frequency waveform effects and to what extent ray theoretical predictions are a useful

754 approximation. Despite these limitations, we expect that future work that predicts body
755 wave observations in the presence of lowermost mantle anisotropy in a finite-frequency
756 framework will likely find similar results: a diversity of seismic phases and measurement
757 yields the best probability of capturing the symmetry, orientation, and properties of an
758 elastic tensor. While this study is limited to a specific set of currently-available elastic
759 tensors from the mineral physics literature, our overall findings should be generally
760 applicable and adaptable to future improvements of our knowledge of lowermost mantle
761 elasticity.

762

763 **5. Summary**

764 To summarize, the complete characterization and interpretation of seismic
765 anisotropy at the base of the mantle would have profound effects on our understanding of
766 lower mantle dynamics, potentially yielding insights into the pattern of mantle flow. Many
767 recent studies have pointed to the difficulty of distinguishing different models of lowermost
768 mantle anisotropy with body wave observations, given challenges with data coverage and
769 uncertainties in the mechanism for anisotropy and the relationships between deformation
770 and the resulting anisotropy at lower mantle conditions. In this study, we conducted a series
771 of Monte Carlo simulations to determine what combination of body wave datasets (shear
772 wave splitting and reflection polarities) are required to constrain D'' anisotropy. We tested
773 various starting models, orientations, and methods for the detection and identification of
774 D'' anisotropy. The modeling approach in this study is applicable to a wide range of
775 elasticity models, and can be extended as our knowledge of the physical properties of the

776 lowermost mantle increases. This approach can be used in future work on D'' anisotropy to
777 further explore how well a dataset can discriminate among possible elastic tensors.

778 Our results show that a diversity of observational techniques, including different
779 types of seismic phases propagating over a range of raypath directions, are necessary in
780 order to maximize the chances of constraining anisotropy at the base of the mantle. A
781 combination of shear wave splitting measurements and observations of PdP and SdS
782 reflection polarities in the same regions may be particularly powerful. We have further
783 shown that if the mineralogy and/or mechanism for anisotropy can be constrained from
784 independent data, then the orientation of the elastic tensor (and thus information about
785 patterns of mantle flow) can likely be retrieved from observational datasets that include a
786 relatively modest number of measurements.

787 **Tables**

788 Table 1

789 Summary of all elastic tensors used in the forward modeling. Columns show the type of
 790 tensor (single-crystal, LPO based on experimental data, SPO based on effective medium
 791 averaging, or LPO based on global flow and texture models), the phases and/or
 792 constituents, and the reference. For the single-crystal tensors, the pressure and temperature
 793 conditions used in the modeling are also indicated. ¹Elastic tensors used for tests to
 794 uniquely constrain the starting model. ²Elastic tensors used for tests to uniquely constrain
 795 the orientation.

Single Crystal Tensors				
Geometry	Phase	Pressure (GPa)	Temperature (K)	References
Single Crystal	Br ¹	125	2500	<i>Wentzcovitch et al.</i> [2006], <i>Wookey et al.</i> [2005a, 2005b]
		126	2800	
		136	4000	
	Ppv ^{1,2}	135	4000	<i>Stackhouse et al.</i> [2005]
	MgO ¹	135	3000	<i>Karki et al.</i> [1999]
Other Tensors				
Geometry	Phase	Notes	References	
Experimental LPO	MgO ¹	P = 0.3 GPa; T = 1473K	<i>Long et al.</i> [2006]	
SPO ¹	0.003 vol. fraction melt	Oblate shape	<i>Walker and Wookey</i> [2012]	
	0.003 vol. fraction melt	Tubule shape	<i>Walker and Wookey</i> [2012]	
Calculated LPO ²	Ppv	TX2008-V1 model; dominant slip plane: (010), P = 125-136; T = 3000-4000 K	<i>Walker et al.</i> [2011]; Tensors based on <i>Stackhouse et al.</i> , [2005] and <i>Stackhouse and Brodholt</i> [2007]	

796

797

798

799 Table 2

800 Models for the top (isotropic) and bottom (anisotropic) layers of each model described in
 801 Figure 3 for reflection polarity models. The dominant slip system assumed in each bottom
 802 layer is listed.

Model	Top Layer (isotropic)	Bottom Layer (anisotropic)	Slip System	References
A	Ppv	Ppv	[100](010)	<i>Walte et al. [2009]</i> <i>Wentzcovitch et al. [2006]</i>
B	Br	Ppv	[100](010)	<i>Walte et al. [2009]</i> <i>Wentzcovitch et al. [2006]</i>
C	Br	Br	[010](100)	<i>Stackhouse et al. [2005]</i> <i>Mainprice et al. [2008]</i>
D	Fp	Fp	[100](001)	<i>Karki et al. [1999]</i>

803

804

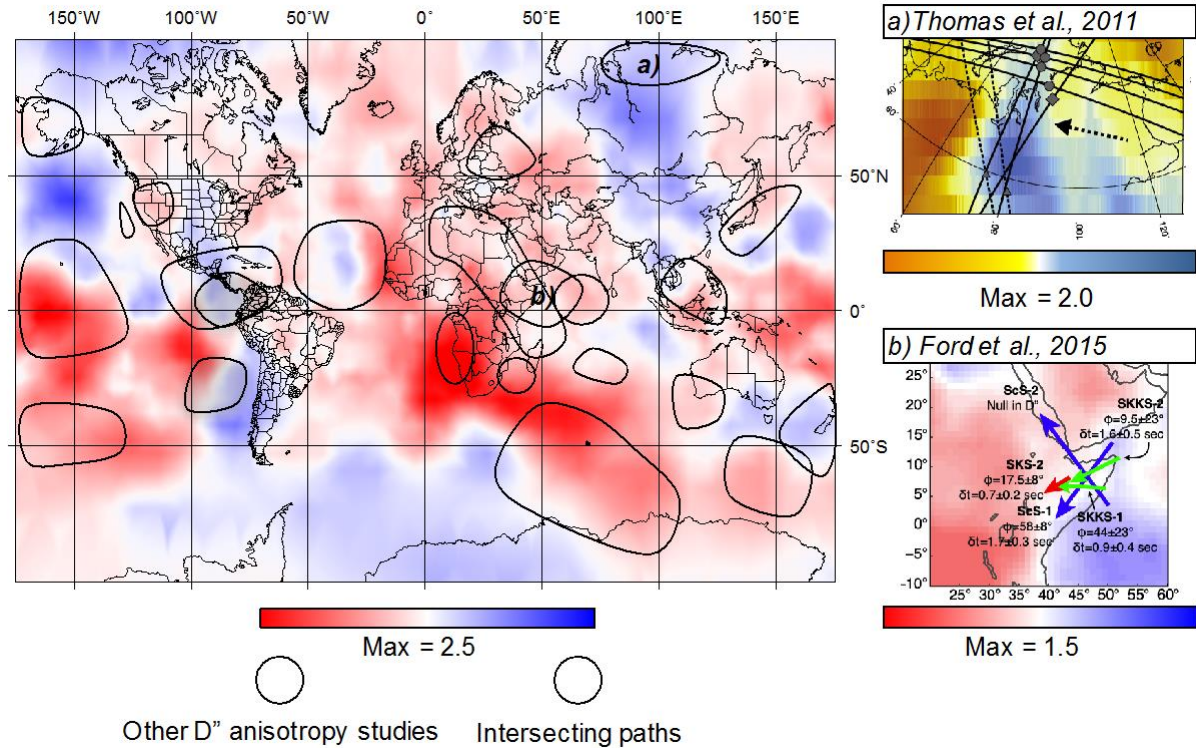
805 Table 3

806 Summary of previous studies that have used crossing raypaths to study D'' anisotropy, as
 807 identified in Figure 1. The number of unique azimuths is given; each azimuth typically
 808 contains multiple observations (in practice, these observations are typically averaged for
 809 each set of raypaths). SKS number is calculated as defined in the text; for example,
 810 Nowacki et al. (2010) used only ScS phases, therefore the SKS number is 0. Angular
 811 dispersion (R) of the raypath azimuths is also calculated as described in the text.

References	Region	Number of Unique Azimuths	SKS Number	R
Creasy et al., 2017	New Zealand	8	0.75	0.7866
Creasy et al., 2017	SW Australia	4	0.5	0.4297
Ford et al., 2015	Afar Peninsula	5	0.6	0.8305
Thomas et al., 2011	Siberia + Caribbean	4	reflection polarities	0.5801
Nowacki et al., 2010	Caribbean	6	0	0.5734

812

813 **Figure Captions**



814

815

816 Figure 1. Summary map of previously published studies (which include shear wave
817 splitting measurements and reflection polarity observations) to constrain D'' anisotropy,
818 updated and adapted from Nowacki et al. (2011). Highlighted areas (pink/gray) indicate
819 regions that have been probed for D'' anisotropy with these methods. Regions in pink
820 indicate studies that used multiple techniques and/or intersecting ray paths, for which at
821 least two observations intersect in the same region with different propagation azimuths.
822 Two such studies are highlighted on the right. Panel (a) shows the raypaths (black lines)
823 beneath Siberia studied in the reflection polarity study of Thomas et al. (2011). CMB
824 bounce points are indicated with diamonds and circles, and the dotted arrow indicates paleo
825 subduction direction 100 Ma ago of the Kula plate. Background colors indicate P wave
826 velocity deviations at the base of the mantle from the model of Kárason and Hilst (2001).

827 Panel (b) shows a schematic diagram of shear wave splitting measurements of SKS (green),
828 SKKS (red) , and ScS (blue) phases beneath the Afar region of Africa (Ford et al., 2015).
829 Background colors show S wave velocity deviations at a depth of 250 km above core
830 mantle boundary from the GyPSuM tomography model (Simmons et al., 2010). Color
831 scales indicate the maximum S or P wave velocity deviation.

832

833

834

835

836

837

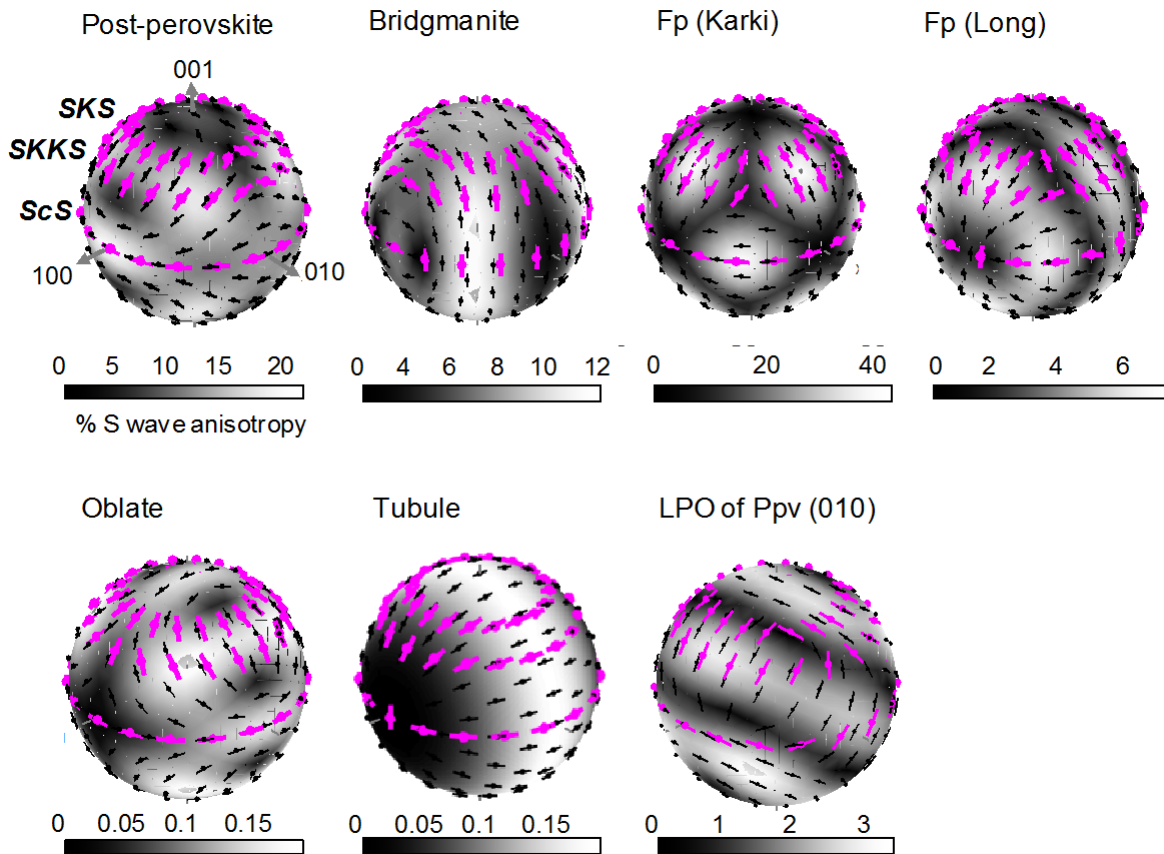
838

839

840

841

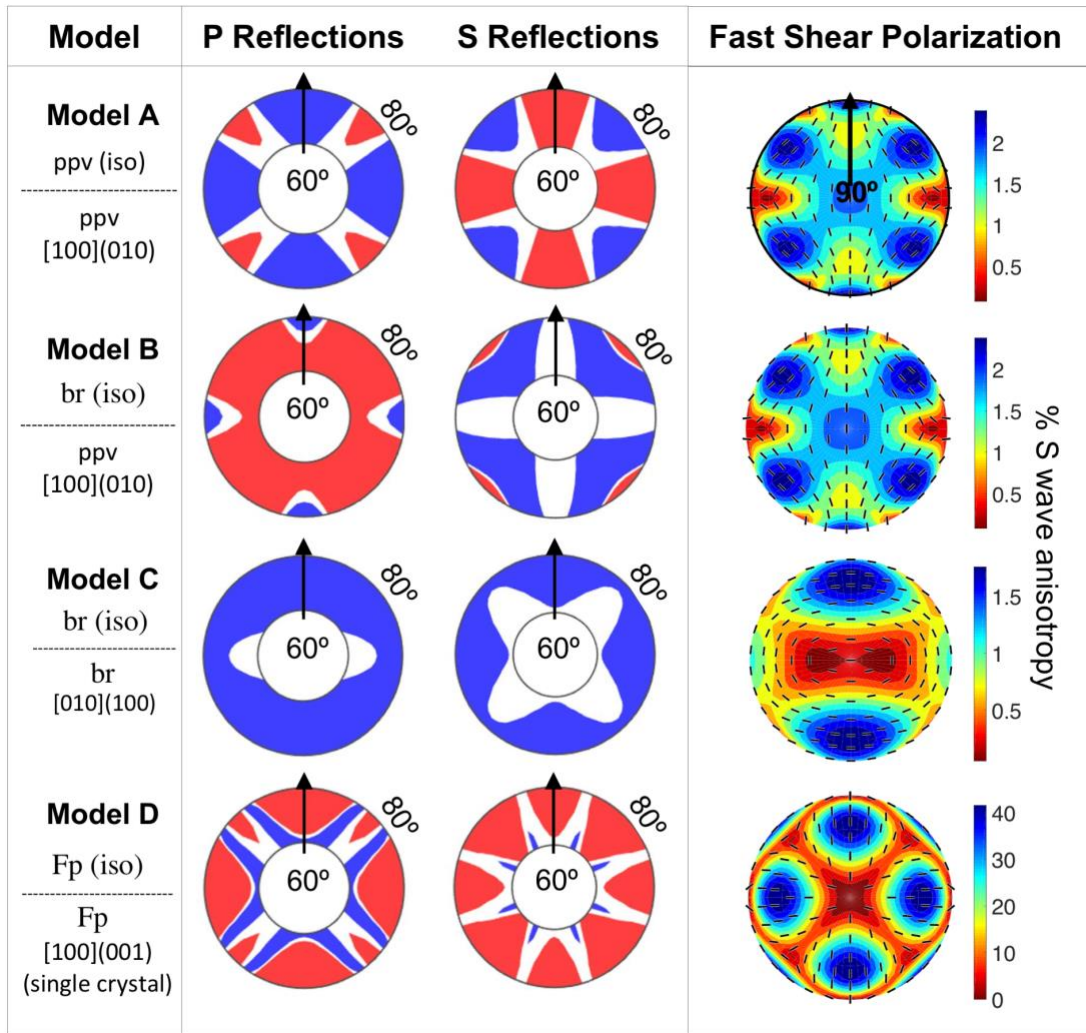
842



843

844 Figure 2. Elastic properties of models from Table 1 for D'' anisotropy tested in this
 845 study, as expressed in the predicted shear wave splitting behavior. Predicted shear wave
 846 splitting behavior is shown as a 3D spherical representation relative to geographic space,
 847 with the [100], [010], and [001] axes indicated in order to view the variation of splitting of
 848 SKS, SKKS, and ScS with azimuth. The anisotropy 3-D spheres show the directional
 849 dependence of seismic anisotropy (strength [gray color bar] and fast-axis directions [black
 850 bars]). For each model, the [100] and [010] axes are parallel to the CMB and oriented north
 851 and west, respectively. Black bars show predicted splitting over a range inclinations and
 852 azimuths, as computed using the MSAT toolkit (Walker and Wookey, 2012). Magenta bars
 853 illustrate the predicted fast polarization directions for the given starting models for a
 854 particular set of SKS, SKKS, and ScS raypaths every 20° (we actually use steps of 5° in

855 the synthetic modeling, but the plotting is too dense to show) that are evenly distributed.
856 Inclination angles used in the modeling are based on the average inclination angles for each
857 phase through the D" layer; we assume that ScS propagates nearly horizontally through the
858 lowermost mantle, as described in the text. From left to right, we show elastic tensor models
859 for single-crystal Ppv (Stackhouse et al., 2005), single-crystal Br (Wentzcovitch et al.,
860 2006), single-crystal Fp (Karki et al., 1999: Labeled as "Fp (Karki)"), experimentally-
861 derived LPO of Fp (Long et al., 2006: Labeled as "Fp (Long)"), Oblate SPO (Walker and
862 Wookey, 2012), Tubule SPO (Walker and Wookey, 2012), and the averaged, textured Ppv
863 (Walker et al., 2011). Background colors are %S-wave anisotropy.
864



865

866 Figure 3. Predictions of reflection polarities for PdP and SdS waves for different
867 D'' anisotropy models shown as an upper hemispherical projection since polarities depend
868 on azimuth, not inclination as in Figure 2. Predictions are made as a function of azimuth
869 and epicentral distance (from 60° to 80°). Azimuth is relative to the slip direction (indicated
870 by the black arrow), which also corresponds to direction of lowermost mantle flow for a
871 simple horizontal shear geometry. The first two columns show the reflection coefficients
872 of P-P and SH-SH upon reflection off the D'' discontinuity, located 300 km above the core
873 mantle boundary in the model. Blue and red regions indicate positive and negative
874 polarities, respectively. Models A, C, and D illustrate situations where there is an onset of

875 anisotropy at the D" discontinuity while Model B invokes both a phase change (from Br to
876 Ppv) and the onset of anisotropy. The last column illustrates the predicted S wave
877 anisotropy (color bar) and predicted shear wave splitting fast directions (black bars) for the
878 same models, plotted as a function of azimuth and inclination from the horizontal. Elastic
879 tensors corresponding to these models are shown in Table 2.

880

881

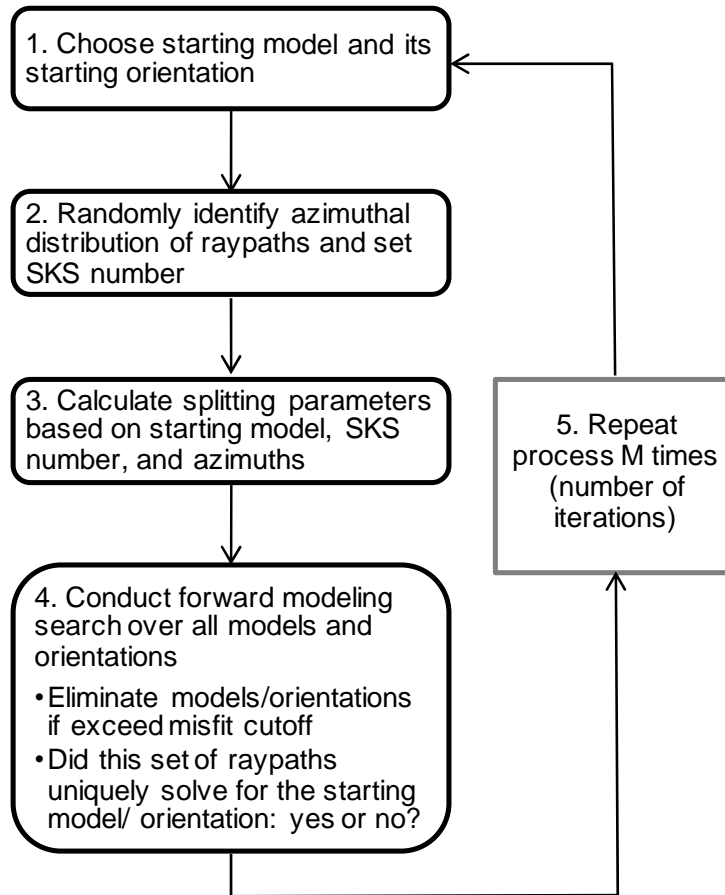
882

883

884

885

886

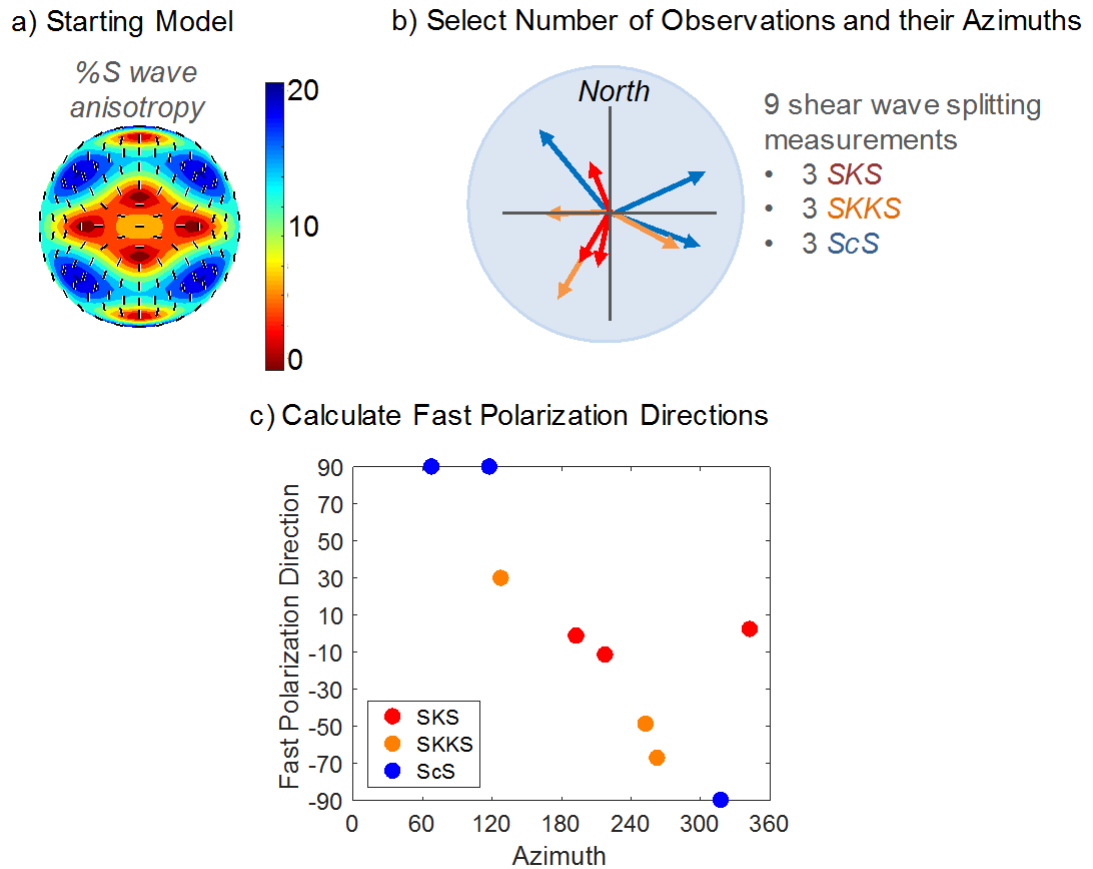


887

888 Figure 4. Flow chart of steps in our modeling framework. The first step is to identify
 889 the starting model and its orientation from Tables 1 or 2. Secondly, randomly choose an
 890 azimuthal distribution of raypaths through the starting model and fix the SKS number.
 891 Thirdly, use the raypaths from step 2 and calculate the fast polarization directions and/or
 892 reflection polarities (splitting parameters) based on the identified starting model and SKS
 893 number. Fourth, use this synthetic dataset to use the forward modeling approach to identify
 894 which models and orientations fit the synthetic dataset. We apply the misfit cutoff as
 895 described in Methods to eliminate certain models and orientations in order to see if the
 896 synthetic dataset can uniquely constrain the starting model. Lastly, in step 5, we repeat this

897 same process M times (number of iterations), identifying a new random distribution of
898 raypaths each time.

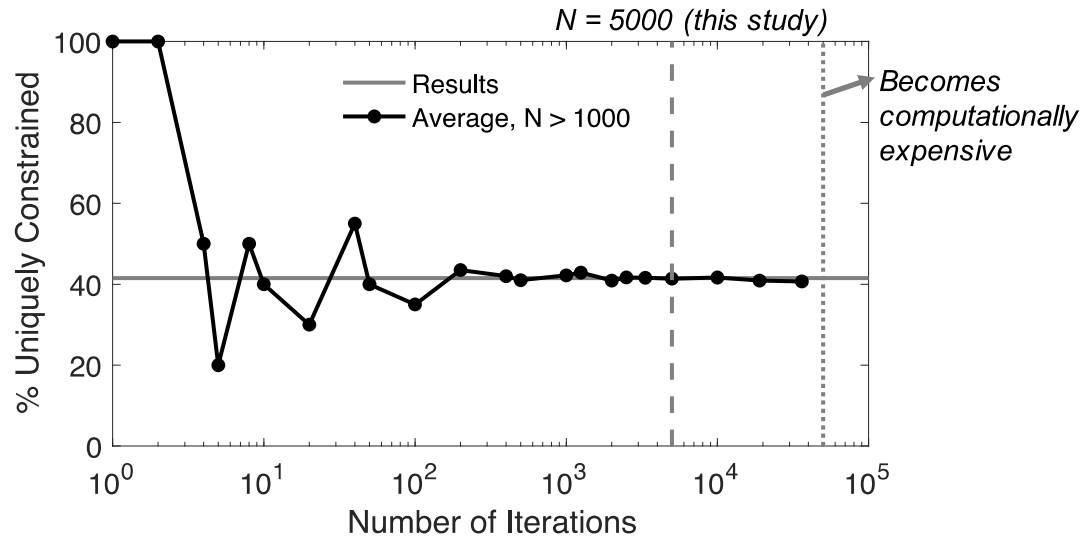
899



900

901 Figure 5. An illustrative example of how shear wave splitting predictions for an
902 individual iteration in our stochastic modeling scheme are calculated. (a) Plane view
903 (looking down from above on CMB) of starting model for Ppv (Stackhouse et al., 2005)
904 showing S wave % anisotropy (colors), with fast polarization directions plotted as black
905 bars. (b) Raypath distribution for this example for SKS (red), SKKS (orange), and ScS
906 (blue), plotted as azimuth from north. (c) The predicted fast polarization directions based
907 on the starting model in (a) and the raypath distribution in (b). Colors indicate phase type.

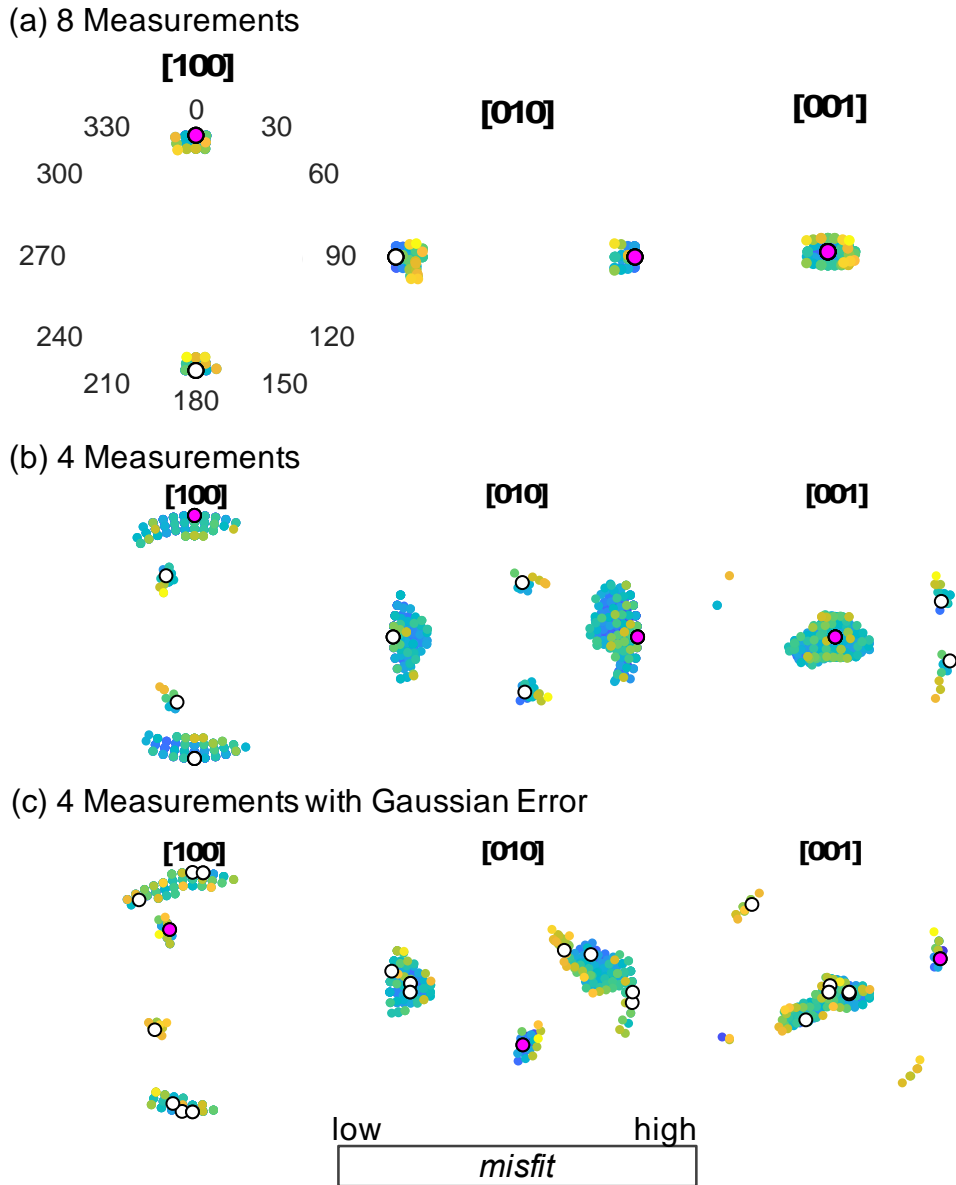
908



910

911 Figure 6. Results of a test of how many iterations are needed for the model results
 912 to converge. The x-axis defines the number of iterations (M) (that is, number of unique
 913 raypath configurations with similar characteristics) that were successively carried out. The
 914 y-axis indicates what percentage of the iterations run could be uniquely constrained. This
 915 particular test used 9 shear wave splitting measurements and a starting model of horizontal
 916 Ppv, and we found that after a large number of iterations, the starting model could be
 917 constrained for 41% of all iterations carried out. In contrast, for the other 59%, a unique
 918 solution of Ppv could not be constrained for that particular synthetic dataset. Based on the
 919 results of this test, at least 5,000 iterations were carried out for each test described in this
 920 study.

921

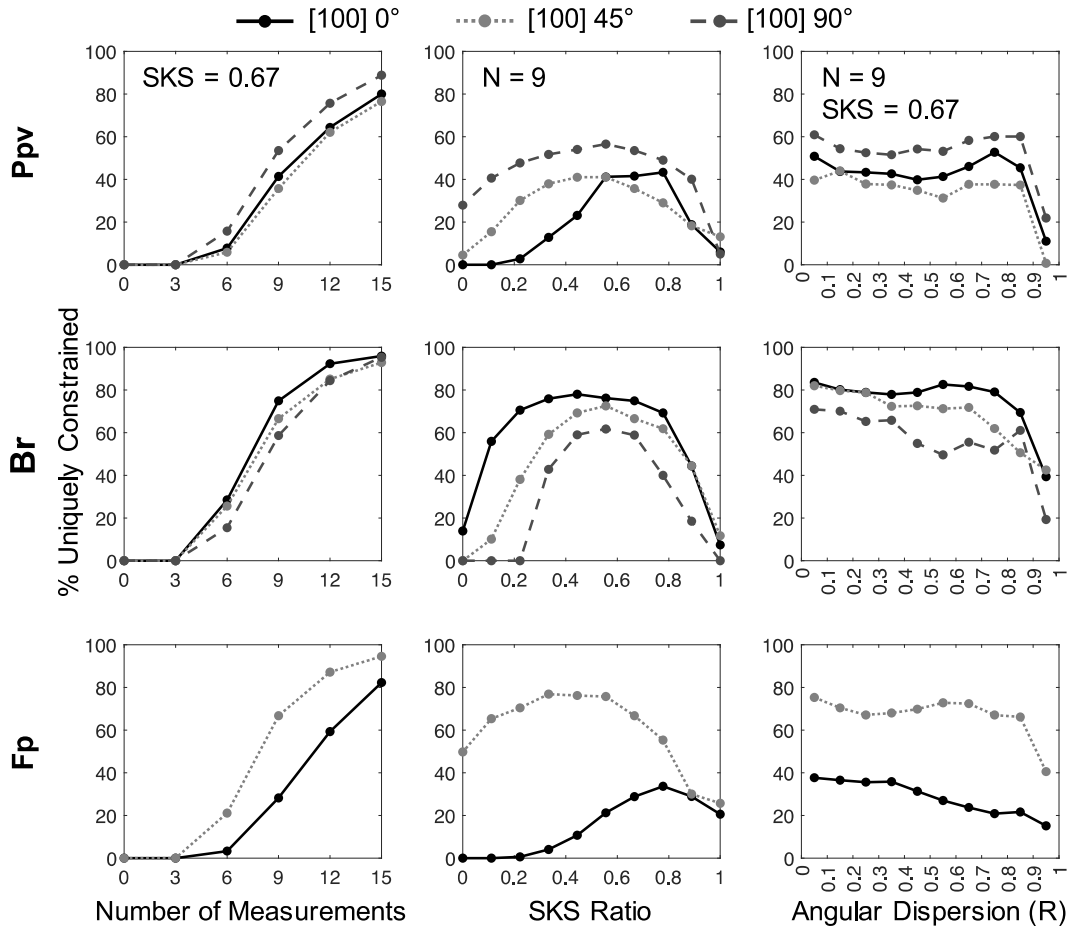


922

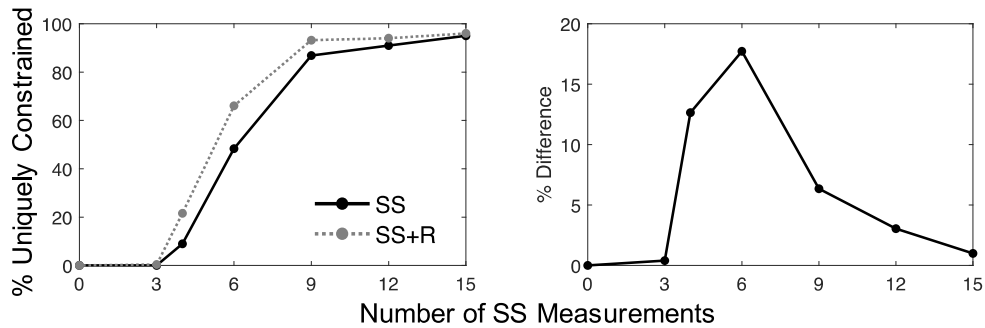
923 Figure 7. An example of how the forward modeling method identifies all possible
 924 orientations of the Ppv single crystal elastic tensor that fit a particular synthetic dataset. We
 925 show two synthetic datasets of 8 (a) and 4 (b) unique synthetic measurements with 3 SKS,
 926 3 SKKS, 2 ScS measurements and 1 SKS, 2 SKKS, and 1 ScS measurements, respectively.
 927 The last case (c) shows a test with the same 4 synthetic measurements as in (b) but with
 928 Gaussian distributed random error to the predicted fast directions. These projections show

929 all possible permissible orientations (colored dots) of the Ppv tensor for the given synthetic
930 dataset plotted as an upper hemispherical projection of the [100], [010], and [001] axes.
931 The white dots mark local minima, where the magenta dots represent the global minimum.
932 The magenta dots indicate the global minimum misfit, which should be equal to a non-
933 rotated Ppv (that is, horizontal [100] and [010] axes and vertical [001] axis).
934

(a) Changes in the Starting Model



(b) Adding 1 Reflection Measurement



935

936

937

938

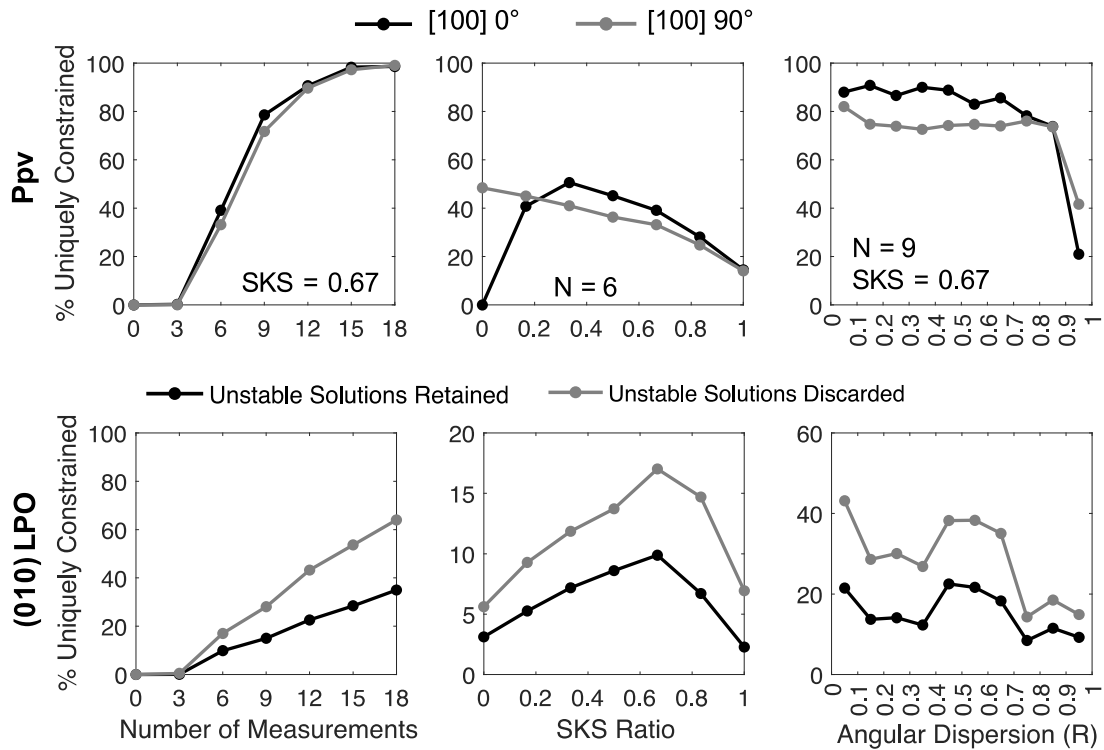
939

Figure 8: Results of synthetic tests that aim to uniquely constrain the starting model/mechanism, as discussed in section 3.2. Three different sets of tensors were tested, while three different aspects of the raypath configuration were varied. In (a), each row shows plots of the probability of uniquely identifying the given starting model (Ppv, Br,

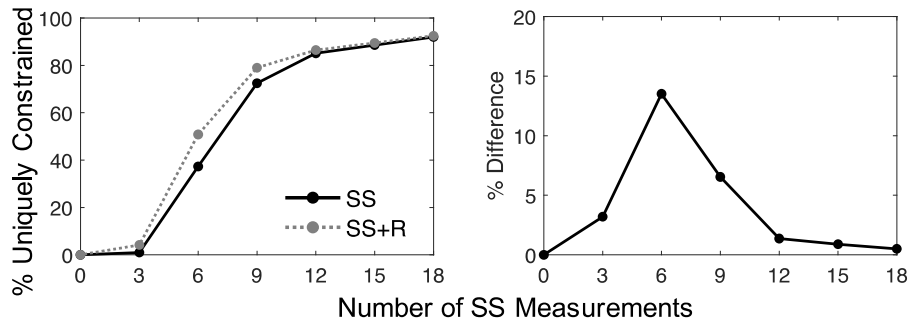
940 and MgO). Each column represents the variable describing raypath configuration that was
941 allowed to vary, while the other two were fixed. In the first column, we varied the number
942 of measurements N , but fixed the SKS ratio (0.67) and tested the full range of possible R
943 values. In the second column, we varied SKS number but fixed the number of
944 measurements ($N = 9$) and tested the full range of possible R values. In the third column,
945 we varied the angular dispersion R , but fixed the number of measurements and SKS
946 number ($N = 9$ and $SKS = 0.6$). We further tested a range of starting orientations for each
947 starting model (three for Ppv and Br, two for Fp); the labels (0, 45, 90) refer to the rotation
948 angle (in degrees) about the [100] axis from the horizontal. In (b), we chose Model A in
949 Figure 3 as the starting model and tested whether we could uniquely constrain this starting
950 model using a combination of shear wave splitting and reflection measurements. For this
951 test, the SKS number was fixed (0.67) and we tested the full range of possible angular
952 dispersion values. The test shown in (b: left image) compares synthetic datasets with only
953 shear wave splitting measurements (black line, SS) to those that include splitting plus one
954 additional reflection measurement for a P and S reflected phase off the D" over a randomly
955 defined azimuth (gray line, SS+R). The difference in probability between these two raypath
956 configuration scenarios is shown in right image.

957

(a) Changes in the Starting Model Orientation



(b) Adding 1 Reflection Measurement



958

959

960

961

962

963

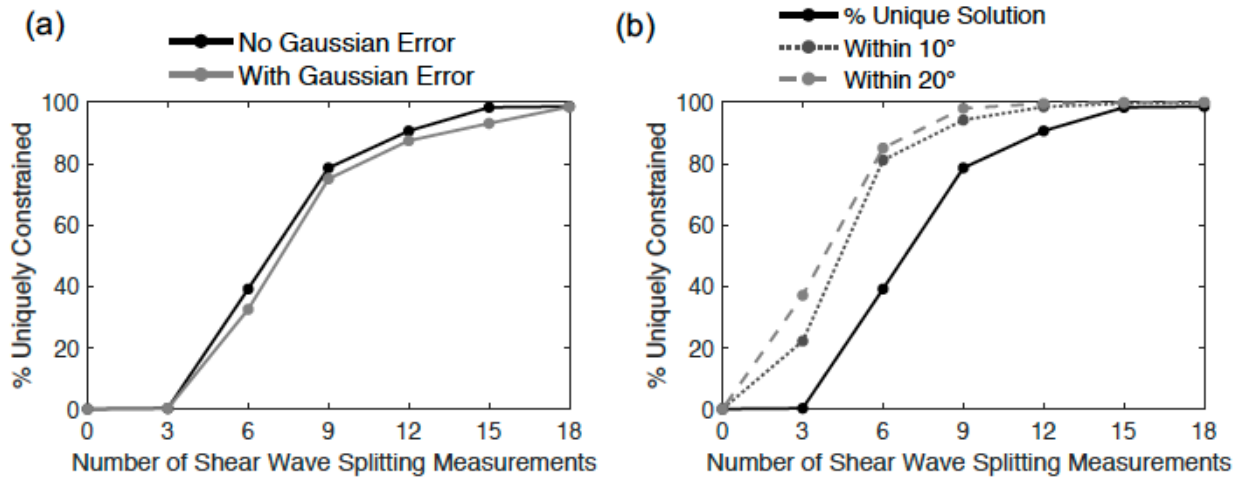
964

Figure 9. Results of synthetic tests that aim to uniquely constrain the orientation of a Ppv starting model, as discussed in section 3.3. In (a), each row shows plots of the probability of uniquely identifying the given starting model's orientation using the synthetic data, for three different orientations about the [100] axis in the starting model, as shown in the legend (with the labels 0 and 90, referring to the angle about the [100] axis) and described in the text. As in Figure 7, each column represents the variable that was

965 allowed to vary, while the other two were fixed. The second row illustrates the results of
966 tests that aimed to uniquely constraining the starting model orientation for textured Ppv
967 models invoking slip on the (010) plane (Walker et al., 2011). For these tests, we
968 distinguish between scenarios in which we increased the sensitivity (that is, discarded
969 “unstable” solutions, as described in the text). Tests in which unstable solutions were
970 discarded (gray line) increased the probability of identifying the orientation of anisotropy
971 in comparison to retaining unstable solutions (black line). In (b), we show results of tests
972 of the effect of adding one additional reflection measurement to the shear wave splitting
973 measurements, using Model A in Figure 3 as the starting model. For these tests, the SKS
974 number was fixed (0.67) and we tested the full range of possible angular dispersion values.
975 The test shown in (b: left image) compares synthetic datasets with only shear wave splitting
976 measurements (black line, SS) to those that include splitting plus one additional reflection
977 measurement for a P and S reflected phase off the D" over a randomly defined azimuth
978 (gray line, SS+R). The difference in probability between these two raypath configuration
979 scenarios is shown at right.

980

981



982

983 Figure 10: Results of tests that aimed to uniquely identify the orientation of a single-

984 crystal Ppv starting model, with Gaussian distributed random errors (standard deviation =

985 9°) incorporated into the synthetic shear wave splitting dataset. In (a), we varied the number

986 of shear wave splitting measurements and calculated the probabilities of correctly

987 retrieving the starting model orientation. In (b), we plot the probability of correctly

988 identifying the starting orientation for a synthetic dataset with Gaussian error applied based

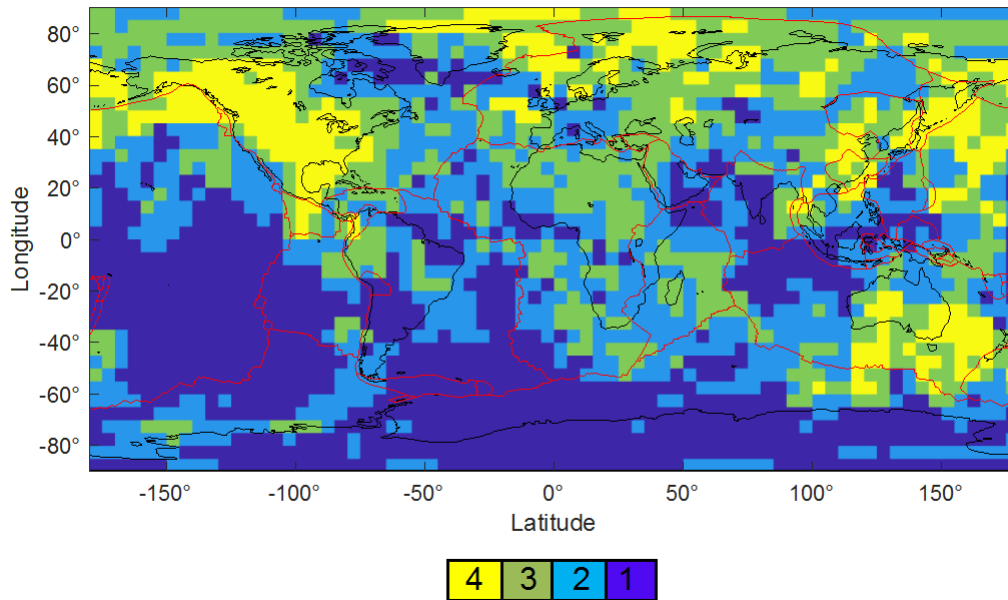
989 on an identification of the minimum misfit (as opposed to searching for a unique solution).

990 In (b), the black line (unique solution, same as in (a)) shows the probability of uniquely

991 constraining the orientation of the starting model. The other two lines show the probability

992 of identifying the correct solution within 10° or 20° by using the minimum misfit.

993



994

995 Figure 11. Map of regions of the lowermost mantle in which the various
 996 measurement methods (SKS [distance range: $108^\circ - 122^\circ$], SKKS [$108^\circ - 122^\circ$], and ScS
 997 [$60^\circ - 80^\circ$] shear wave splitting and reflection polarities) used in this study could
 998 potentially be applied. We parameterize the D'' layer into a 5° by 5° grid. We calculated
 999 raypaths for different seismic phases using TauP (Crotwell et al., 1999) assuming a 250km
 1000 thick D'' layer. We used a set of seismic stations with simple upper mantle anisotropy
 1001 (Lynner and Long, 2013, 2014b) for all events greater than Mw6.5 that occurred in the
 1002 time span of deployment for each seismic station for SKS, SKKS, and ScS. For reflection
 1003 polarities, we considered only dense arrays openly available: TAMNNET, POLENET,
 1004 GAMSEIS, Yellowknife Array, KNET, Southern California Network, GRSN Array, F-
 1005 Net, USArray (using stations in Alaska), USArray (using stations in Texas), USArray
 1006 (using stations in Minnesota), USArray (using stations in New York), USArray (using
 1007 stations in South Carolina), and the Pacific Northwest Seismic Network.

1008

1009 **Acknowledgements**

1010 This work was supported by a National Science Foundation (NSF) Graduate Research
1011 Fellowship grant DGE-1122492 to N.C. and by NSF grant EAR-1547499 to M.D.L. Some
1012 figures were prepared using the Generic Mapping Tools (Wessel and Smith, 1991). We
1013 thank the Yale Center for Research Computing for guidance and use of the research
1014 computing infrastructure, specifically Kaylea Nelson. AP received funding from the
1015 European Union's Horizon 2020 research and innovation program under the Marie
1016 Sklodowska-Curie grant agreement No 642029 - ITN CREEP. We are grateful to Sanne
1017 Cottaar, Jeroen Ritsema, and editor Ana Ferreira for thoughtful and constructive comments
1018 that helped us to improve the paper.

1019

1020

1021 **References**

1022

- 1023 Bendat, J.S., Piersol, A.G., 2011. Random Data: Analysis and Measurement Procedures.
1024 John Wiley & Sons.
- 1025 Cottaar, S., Romanowicz, B., 2013. Observations of changing anisotropy across the
1026 southern margin of the African LLSVP. *Geophys. J. Int.* ggt285.
1027 <https://doi.org/10.1093/gji/ggt285>
- 1028 Creasy, N., Long, M.D., Ford, H.A., 2017. Deformation in the lowermost mantle beneath
1029 Australia from observations and models of seismic anisotropy. *J. Geophys. Res.*
1030 *Solid Earth* 122, 2016JB013901. <https://doi.org/10.1002/2016JB013901>
- 1031 Crotwell, H.P., Owens, T.J., Ritsema, J., 1999. The TauP Toolkit: Flexible Seismic
1032 Travel-time and Ray-path Utilities. *Seismol. Res. Lett.* 70, 154–160.
1033 <https://doi.org/10.1785/gssrl.70.2.154>
- 1034 Deng, J., Long, M.D., Creasy, N., Wagner, L., Beck, S., Zandt, G., Tavera, H., Minaya,
1035 E., 2017. Lowermost mantle anisotropy near the eastern edge of the Pacific
1036 LLSVP: constraints from SKS–SKKS splitting intensity measurements. *Geophys.*
1037 *J. Int.* 210, 774–786. <https://doi.org/10.1093/gji/ggx190>
- 1038 Ford, H.A., Long, M.D., 2015. A regional test of global models for flow, rheology, and
1039 seismic anisotropy at the base of the mantle. *Phys. Earth Planet. Inter.* 245, 71–75.
1040 <https://doi.org/10.1016/j.pepi.2015.05.004>
- 1041 Ford, H.A., Long, M.D., He, X., Lynner, C., 2015. Lowermost mantle flow at the eastern
1042 edge of the African Large Low Shear Velocity Province. *Earth Planet. Sci. Lett.*
1043 420, 12–22. <https://doi.org/10.1016/j.epsl.2015.03.029>
- 1044 Ford R., Garnero Edward J., McNamara Allen K., 2006. A strong lateral shear velocity
1045 gradient and anisotropy heterogeneity in the lowermost mantle beneath the
1046 southern Pacific. *J. Geophys. Res. Solid Earth* 111.
1047 <https://doi.org/10.1029/2004JB003574>
- 1048 Garnero, E.J., McNamara, A.K., Shim, S.-H., 2016. Continent-sized anomalous zones
1049 with low seismic velocity at the base of Earth’s mantle. *Nat. Geosci.* 9, 481–489.
1050 <https://doi.org/10.1038/ngeo2733>
- 1051 Goryaeva, A.M., Carrez, P., Cordier, P., 2017. Modeling defects and plasticity in
1052 MgSiO₃ post-perovskite: Part 3—Screw and edge [001] dislocations. *Phys.*
1053 *Chem. Miner.* 44, 521–533. <https://doi.org/10.1007/s00269-017-0879-0>
- 1054 Groos, J.C., Ritter, J.R.R., 2009. Time domain classification and quantification of seismic
1055 noise in an urban environment. *Geophys. J. Int.* 179, 1213–1231.
1056 <https://doi.org/10.1111/j.1365-246X.2009.04343.x>
- 1057 Guest, W.S., Kendall, J.M., 1993. Modeling seismic waveforms in anisotropic media
1058 using maslov asymptotic theory. *J. Explor. Geophys.* 29, 78–92.
- 1059 Káráson, H., Hilst, R.D. van der, 2001. Tomographic imaging of the lowermost mantle
1060 with differential times of refracted and diffracted core phases (PKP, Pdiff). *J.*
1061 *Geophys. Res. Solid Earth* 106, 6569–6587.
1062 <https://doi.org/10.1029/2000JB900380>
- 1063 Karki, B.B., Wentzcovitch, R.M., Gironcoli, S. de, Baroni, S., 1999. First-Principles
1064 Determination of Elastic Anisotropy and Wave Velocities of MgO at Lower

1065 Mantle Conditions. *Science* 286, 1705–1707.
1066 <https://doi.org/10.1126/science.286.5445.1705>
1067 Kawai, K., Geller, R.J., 2010. The vertical flow in the lowermost mantle beneath the
1068 Pacific from inversion of seismic waveforms for anisotropic structure. *Earth*
1069 *Planet. Sci. Lett.* 297, 190–198. <https://doi.org/10.1016/j.epsl.2010.05.037>
1070 Kendall, J.-M., Silver, P.G., 1998. Investigating Causes of D'' Anisotropy, in: *The Core-*
1071 *Mantle Boundary Region*. American Geophysical Union, Washington D.C., pp.
1072 409–412.
1073 Lay T., Helmberger D.V., 1983. The shear-wave velocity gradient at the base of the
1074 mantle. *J. Geophys. Res. Solid Earth* 88, 8160–8170.
1075 <https://doi.org/10.1029/JB088iB10p08160>
1076 Lee, K.K.M., O'Neill, B., Panero, W.R., Shim, S.-H., Benedetti, L.R., Jeanloz, R., 2004.
1077 Equations of state of the high-pressure phases of a natural peridotite and
1078 implications for the Earth's lower mantle. *Earth Planet. Sci. Lett.* 223, 381–393.
1079 <https://doi.org/10.1016/j.epsl.2004.04.033>
1080 Long Maureen D., Lynner Colton, 2015. Seismic anisotropy in the lowermost mantle
1081 near the Perm Anomaly. *Geophys. Res. Lett.* 42, 7073–7080.
1082 <https://doi.org/10.1002/2015GL065506>
1083 Long, M.D., 2009. Complex anisotropy in D'' beneath the eastern Pacific from SKS–
1084 SKKS splitting discrepancies. *Earth Planet. Sci. Lett.* 283, 181–189.
1085 <https://doi.org/10.1016/j.epsl.2009.04.019>
1086 Long, M.D., Xiao, X., Jiang, Z., Evans, B., Karato, S., 2006. Lattice preferred orientation
1087 in deformed polycrystalline (Mg,Fe)O and implications for seismic anisotropy in
1088 D'' . *Phys. Earth Planet. Inter.* 156, 75–88.
1089 <https://doi.org/10.1016/j.pepi.2006.02.006>
1090 Lynner, C., Long, M.D., 2014a. Lowermost mantle anisotropy and deformation along the
1091 boundary of the African LLSVP. *Geophys. Res. Lett.* 41, 2014GL059875.
1092 <https://doi.org/10.1002/2014GL059875>
1093 Lynner, C., Long, M.D., 2014b. Sub-slab anisotropy beneath the Sumatra and circum-
1094 Pacific subduction zones from source-side shear wave splitting observations.
1095 *Geochem. Geophys. Geosystems* 15, 2262–2281.
1096 <https://doi.org/10.1002/2014GC005239>
1097 Lynner, C., Long, M.D., 2013. Sub-slab seismic anisotropy and mantle flow beneath the
1098 Caribbean and Scotia subduction zones: Effects of slab morphology and
1099 kinematics. *Earth Planet. Sci. Lett.* 361, 367–378.
1100 <https://doi.org/10.1016/j.epsl.2012.11.007>
1101 Mardia, K.V., Jupp, P.E., 2000. *Directional statistics*. Wiley.
1102 McNamara, A.K., Karato, S.-I., van Keken, P.E., 2001. Localization of dislocation creep
1103 in the lower mantle: implications for the origin of seismic anisotropy. *Earth*
1104 *Planet. Sci. Lett.* 191, 85–99. [https://doi.org/10.1016/S0012-821X\(01\)00405-8](https://doi.org/10.1016/S0012-821X(01)00405-8)
1105 Meade, C., Silver, P.G., Kaneshima, S., 1995. Laboratory and seismological observations
1106 of lower mantle isotropy. *Geophys. Res. Lett.* 22, 1293–1296.
1107 <https://doi.org/10.1029/95GL01091>
1108 Mitrovica, J.X., Forte, A.M., 2004. A new inference of mantle viscosity based upon joint
1109 inversion of convection and glacial isostatic adjustment data. *Earth Planet. Sci.*
1110 *Lett.* 225, 177–189. <https://doi.org/10.1016/j.epsl.2004.06.005>

- 1111 Murakami, M., Hirose, K., Kawamura, K., Sata, N., Ohishi, Y., 2004. Post-Perovskite
 1112 Phase Transition in MgSiO₃. *Science* 304, 855–858.
 1113 <https://doi.org/10.1126/science.1095932>
- 1114 Nowacki, A., Wookey, J., 2016. The limits of ray theory when measuring shear wave
 1115 splitting in the lowermost mantle with ScS waves. *Geophys. J. Int.* 207, 1573–
 1116 1583. <https://doi.org/10.1093/gji/ggw358>
- 1117 Nowacki, A., Wookey, J., Kendall, J.-M., 2011. New advances in using seismic
 1118 anisotropy, mineral physics and geodynamics to understand deformation in the
 1119 lowermost mantle. *J. Geodyn.* 52, 205–228.
 1120 <https://doi.org/10.1016/j.jog.2011.04.003>
- 1121 Nowacki, A., Wookey, J., Kendall, J.-M., 2010. Deformation of the lowermost mantle
 1122 from seismic anisotropy. *Nature* 467, 1091–1094.
 1123 <https://doi.org/10.1038/nature09507>
- 1124 Parisi, L., Ferreira, A.M.G., Ritsema, J., 2018. Apparent Splitting of S Waves
 1125 Propagating Through an Isotropic Lowermost Mantle. *J. Geophys. Res. Solid*
 1126 *Earth* 123. <https://doi.org/10.1002/2017JB014394>
- 1127 Simmons, N.A., Forte, A.M., Boschi, L., Grand, S.P., 2010. GyPSuM: A joint
 1128 tomographic model of mantle density and seismic wave speeds. *J. Geophys. Res.*
 1129 *Solid Earth* 115, B12310. <https://doi.org/10.1029/2010JB007631>
- 1130 Simmons, N.A., Forte, A.M., Grand, S.P., 2009. Joint seismic, geodynamic and mineral
 1131 physical constraints on three-dimensional mantle heterogeneity: Implications for
 1132 the relative importance of thermal versus compositional heterogeneity. *Geophys.*
 1133 *J. Int.* 177, 1284–1304. <https://doi.org/10.1111/j.1365-246X.2009.04133.x>
- 1134 Simmons, N.A., Myers, S.C., Johannesson, G., Matzel, E., Grand, S.P., 2015. Evidence
 1135 for long-lived subduction of an ancient tectonic plate beneath the southern Indian
 1136 Ocean. *Geophys. Res. Lett.* 42, 2015GL066237.
 1137 <https://doi.org/10.1002/2015GL066237>
- 1138 Stackhouse, S., Brodholt, J.P., Wookey, J., Kendall, J.-M., Price, G.D., 2005. The effect
 1139 of temperature on the seismic anisotropy of the perovskite and post-perovskite
 1140 polymorphs of MgSiO₃. *Earth Planet. Sci. Lett.* 230, 1–10.
 1141 <https://doi.org/10.1016/j.epsl.2004.11.021>
- 1142 Thomas, C., Wookey, J., Brodholt, J., Fieseler, T., 2011a. Anisotropy as cause for
 1143 polarity reversals of D'' reflections. *Earth Planet. Sci. Lett.* 307, 369–376.
 1144 <https://doi.org/10.1016/j.epsl.2011.05.011>
- 1145 Thomas, C., Wookey, J., Simpson M., 2007. D'' anisotropy beneath Southeast Asia.
 1146 *Geophys. Res. Lett.* 34. <https://doi.org/10.1029/2006GL028965>
- 1147 Walker, A.M., Forte, A.M., Wookey, J., Nowacki, A., Kendall, J.-M., 2011. Elastic
 1148 anisotropy of D'' predicted from global models of mantle flow. *Geochem.*
 1149 *Geophys. Geosystems* 12, Q10006. <https://doi.org/10.1029/2011GC003732>
- 1150 Walker, A.M., Wookey, J., 2012. MSAT—A new toolkit for the analysis of elastic and
 1151 seismic anisotropy. *Comput. Geosci.* 49, 81–90.
 1152 <https://doi.org/10.1016/j.cageo.2012.05.031>
- 1153 Walte, N.P., Heidelbach, F., Miyajima, N., Frost, D.J., Rubie, D.C., Dobson, D.P., 2009.
 1154 Transformation textures in post-perovskite: Understanding mantle flow in the D''
 1155 layer of the Earth. *Geophys. Res. Lett.* 36, L04302.
 1156 <https://doi.org/10.1029/2008GL036840>

- 1157 Wang, Y., Wen, L., 2007. Geometry and P and S velocity structure of the “African
1158 Anomaly.” *J. Geophys. Res. Solid Earth* 112, B05313.
1159 <https://doi.org/10.1029/2006JB004483>
- 1160 Wentzcovitch, R.M., Tsuchiya, T., Tsuchiya, J., 2006. MgSiO₃ postperovskite at D''
1161 conditions. *Proc. Natl. Acad. Sci. U. S. A.* 103, 543–546.
1162 <https://doi.org/10.1073/pnas.0506879103>
- 1163 Wookey, J., Kendall, J.-M., 2008. Constraints on lowermost mantle mineralogy and
1164 fabric beneath Siberia from seismic anisotropy. *Earth Planet. Sci. Lett.* 275, 32–
1165 42. <https://doi.org/10.1016/j.epsl.2008.07.049>
- 1166 Wookey, J., Kendall, J.-M., Rumpker, G., 2005a. Lowermost mantle anisotropy beneath
1167 the north Pacific from differential S—ScS splitting. *Geophys. J. Int.* 161, 829–
1168 838. <https://doi.org/10.1111/j.1365-246X.2005.02623.x>
- 1169 Wookey, J., Stackhouse, S., Kendall, J.-M., Brodholt, J., Price, G.D., 2005b. Efficacy of
1170 the post-perovskite phase as an explanation for lowermost-mantle seismic
1171 properties. *Nature* 438, 1004–1007. <https://doi.org/10.1038/nature04345>
- 1172 Yamazaki, D., Yoshino, T., Ohfuji, H., Ando, J., Yoneda, A., 2006. Origin of seismic
1173 anisotropy in the D'' layer inferred from shear deformation experiments on post-
1174 perovskite phase. *Earth Planet. Sci. Lett.* 252, 372–378.
1175 <https://doi.org/10.1016/j.epsl.2006.10.004>
1176

1 **Supplemental Material:**

2
3 **Constraining lowermost mantle anisotropy with body waves: A synthetic modeling study**

4
5 Neala Creasy^{1*}, Angelo Pisconti², Maureen D. Long¹, Christine Thomas², and James
6 Wookey³

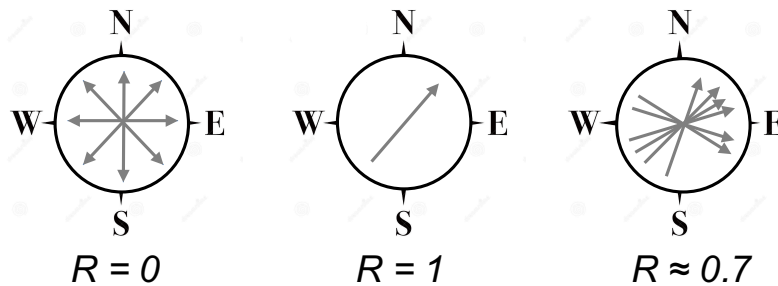
7
8 ¹Department of Geology and Geophysics, Yale University

9 ²Institut für Geophysik, Universität Münster

10 ³Department of Earth Sciences, University of Bristol

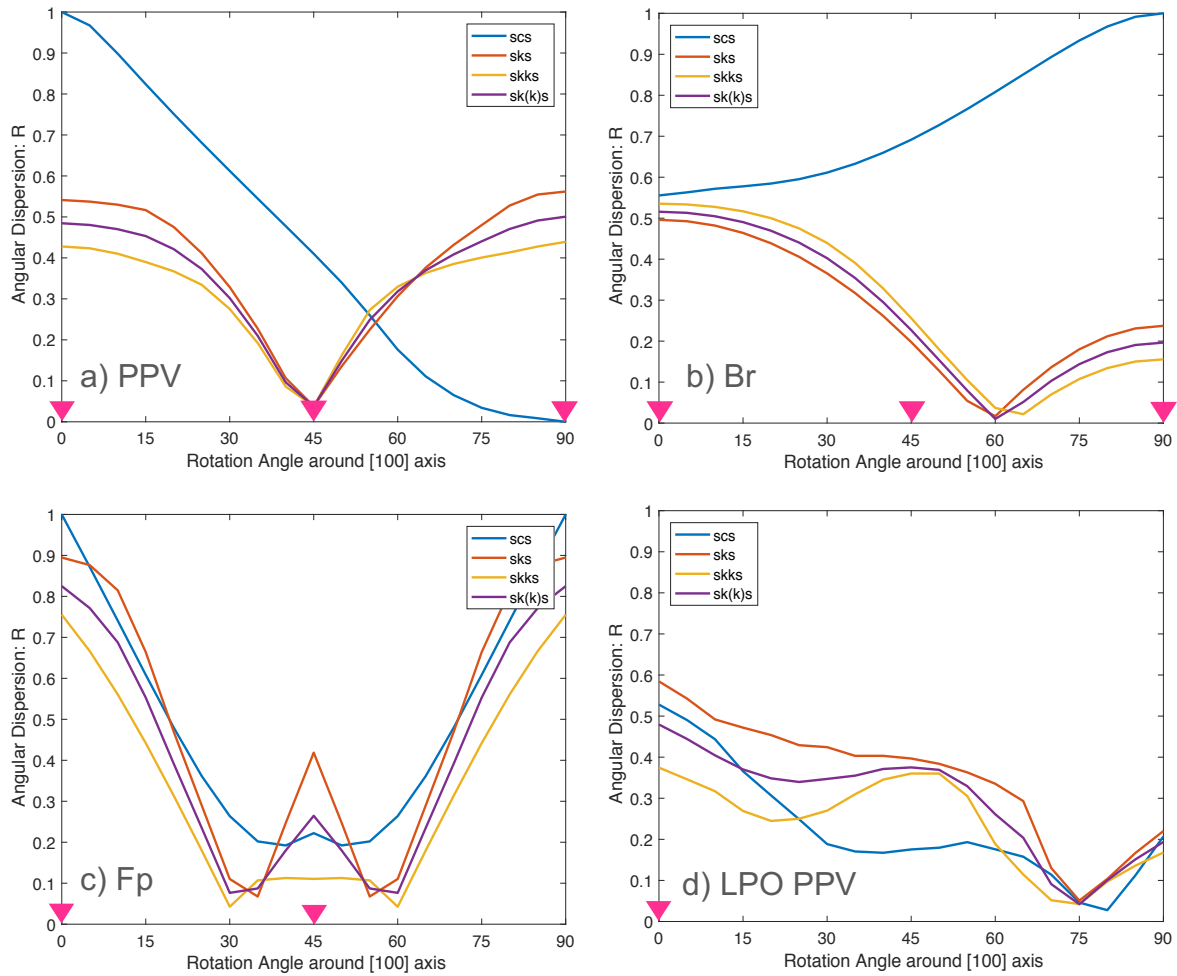
11 *Corresponding author. Email: neala.creasy@yale.edu

12
13 **Supplement Figures**



17 Figure S1. Schematic diagram showing the definition of angular dispersion (R), with
18 arrows indicating a direction anywhere from 0° to 360° . Small values of R indicate a wide
19 distribution of directions, while larger values indicate a tight configuration.

20



21

22

23

24

25

26

27

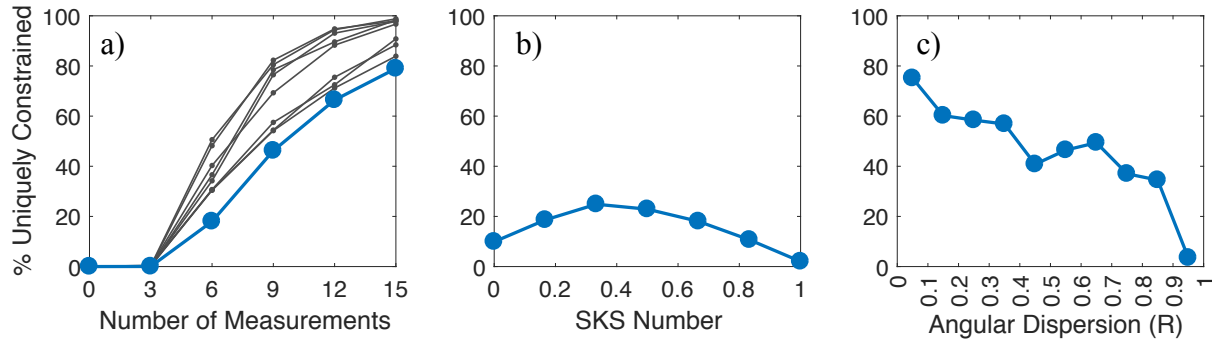
28

29

30

Figure S2. Angular dispersion – R – plots of all predicted fast axis directions for SKS (red), SKKS (orange), SKS and SKKS (violet), and ScS (blue). Equations (2) and (3) from the main text were used to calculate R; however, since fast axis directions can only vary from -90° to 90° , the fast axis orientations were adjusted from -90 to 90 to 0 to 360 . Angular dispersion is plotted in terms of the clockwise rotation angle about the [100] axis of (a) post-perovskite (PPV), (b) bridgmanite (Br), (c) ferropericlase (Fp), and (d) LPO of PPV of the given models, respectively. Magenta triangles indicate the starting models' orientations used in the modeling in the main text as in Figures 8 and 9.

31



32

33

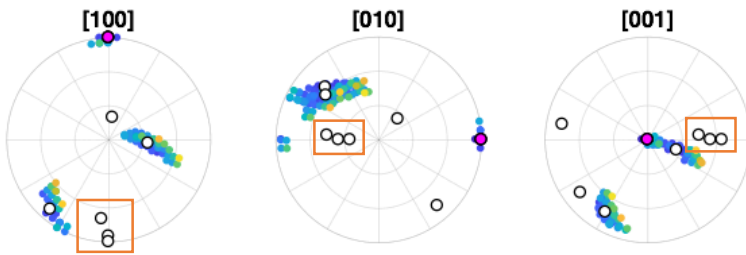
34 Figure S3. Results of synthetic tests that aim to uniquely constrain the orientation of a Ppv
35 starting model, as discussed in section 3.3 in the main text, by selecting 9 random the starting
36 orientations of the Ppv tensor. Each figure illustrates the probability of uniquely identifying the
37 given starting model's orientation using the synthetic data, for nine different orientations of Ppv.
38 As in Figure 7, each column represents the variable that was allowed to vary, while the other two
39 were fixed. For (a), the SKS number was fixed (0.67). For (b), the number of measurements was
40 fixed to six. For (c), the number of measurements was fixed to nine measurements and an SKS
41 number of 0.67. The blue lines in (b) and (c) correlate to the blue line in (a), where the variation
42 of SKS number and angular dispersion were only tested for one of the starting model orientations.

43

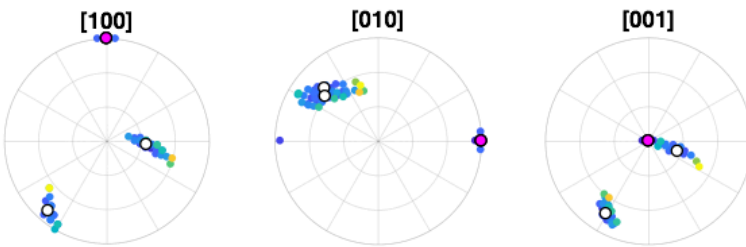
44



Cutoff = 20°

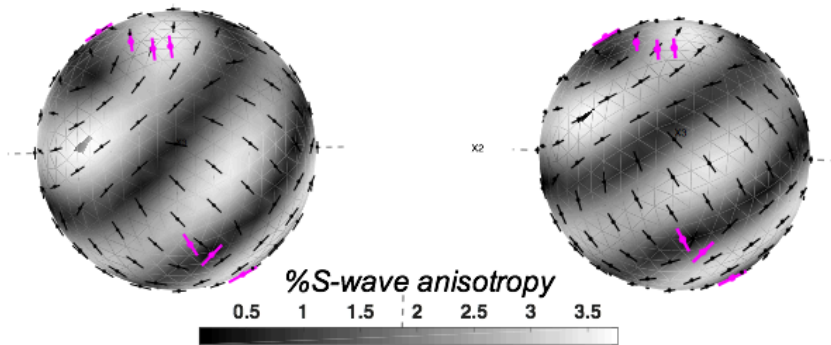
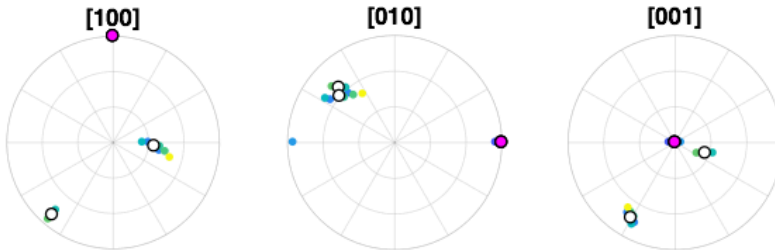


Cutoff = 15°



45

Cutoff = 10°



46

Unstable solution

Unstable solution rotated by 5
degrees, which fails the misfit
criterion

47

48

49 Figure S4: Example illustrating the identification of unstable solutions in a test that aimed
50 to identify the starting orientation of a horizontal textured Ppv LPO. The polar plots show all
51 possible orientations that fit a given synthetic dataset. The colors represent misfit values. The white
52 circles mark the minimum misfit of each cluster of possible orientations. The magenta circles show
53 the correct solution. The orange boxes highlight some of the unstable solutions. Each row
54 represents a different misfit cutoff. The top row represents the cutoff used in this study (20°). The
55 second row uses a cutoff of 15° and the third row 10° . With a lower cutoff, the unstable solutions
56 are eliminated. The bottom elastic tensors on the left show an example of one of the resulting
57 unstable solution from the orange boxes in the first row. The elastic tensor on the right shows the
58 same tensor but rotated by 5° , which fails the misfit criterion. The magenta lines represent the
59 measurements used in this simulation. Colors here represent %S wave anisotropy.

60